Received 17 November 2020; accepted 28 November 2020. Date of publication 2 December 2020; date of current version 28 December 2020.

*Digital Object Identifier 10.1109/OJCOMS.2020.3041930*

# Visible Light Communications via Intelligent Reflecting Surfaces: Metasurfaces vs Mirror Arrays

**AMR M. ABDELHADY (Graduate Student Member, IEEE), AHMED K. SULTAN SALEM (Senior Member, IEEE), OSAMA AMIN (Senior Member, IEEE), BASEM SHIHADA (Senior Member, IEEE), AND MOHAMED-SLIM ALOUINI (Fellow, IEEE)**

Computer Electrical, and Mathematical Science and Engineering Division, King Abdullah University of Science and Technology, Thuwal 6900, Saudi Arabia

CORRESPONDING AUTHOR: B. SHIHADA (e-mail: basem.shihada@kaust.edu.sa)

**ABSTRACT** We propose two types of intelligent reflecting systems based on programmable metasurfaces and mirrors to focus the incident optical power towards a visible light communication receiver. We derive the required phase gradients for the metasurface array reflector and the required orientations of each mirror in the mirrors array reflector to achieve power focusing. Based on which, we derive the irradiance expressions for the two systems in the detector plane to characterize their performance in terms of aiming and focusing capabilities. We show analytically that the number of reflecting elements along with the relative source - reflector dimensions determine the system power focusing capability. Moreover, we quantify analytically the received power gain compared with reflector-free systems. In addition, we introduce a new simple metric to assess the relative reflectors' performance for a given source, detector, reflector layout. Finally, we verify the analytical findings regarding absolute and relative reflectors' performance via numerical simulations.

**INDEX TERMS** Channel modeling, intelligent reflecting surfaces, metasurfaces, mirror arrays, visible light communications.

## I. INTRODUCTION

IN THE past decade, the wireless communications world has experienced not only a quantitative growth but also a qualitative one. As the number of the connected devices increases exponentially, the network capacity and coverage should meet such an expected tremendous growth. Moreover, communication networks have to deliver enhanced mobile services with ultra-reliable low latency communications. Under the 5G umbrella, many research efforts have been dedicated to realizing these ambitions, which was successfully translated into the first 5G standard in June 2018. Nevertheless, the rise of new services as extended reality, holographic communication, connected autonomous systems, tactile interactions motivates researchers to propose unconventional communication networks. Recently, improved thrust research efforts are adopted to formulate visions for 6G networks and their enabling candidate technologies [1], [2].

The main research focus of communications link design has been on optimizing transmitter and receiver structures and operations based on imposed channel conditions. Recently, adding design degrees of freedom to the channels by incorporating tunable intelligent reflecting surfaces (IRSs), has received significant research attention in radio frequency (RF) systems [3]–[5]. Many efforts have been dedicated to model and study the potential gains of using such devices in RF networks performance enhancement [6], [7]. As for the VLC systems, IRSs are expected to participate effectively in boosting their performance, especially that most of the VLC systems rely on the existence of a line of sight (LoS) [8]–[10]. The incorporation of IRSs in indoor VLC systems can provide significant gains in terms of resilience to LoS blockages between the transmitter and the receiver, an improved tradeoff between lighting and communications quality of service, interference mitigation, more efficient

energy harvesting capabilities, and enhanced localization services.

Recently, few efforts are spent on studying intelligent surfaces for optical communication systems [11]–[15]. Najafi and Schober studied using smart mirrors to relax the LoS requirement for FSO links in [11]. Moreover, in [12], Valagiannopoulos added programmable directivity to the transmitter by covering it with a metasurface. In addition, in [13], Cao *et al.* proposed a beam-shaping system at the transmitter to enable non-line of sight VLC using coherent optical transmitter array. In [14], Deng *et al.* proposed and demonstrated a reconfigurable mirco-mirrors based beam-steering system for FSO inter-rack networks of data centers. Furthermore, in [15], Zou *et al.* proposed the use of tunable metasurfaces for inter/intra optical wireless chip communications. In the aforementioned studies, IRSs were realized by either metasurfaces or controllable mirrors. Metasurfaces are synthesized materials composed of arrangements of sub-wavelength metallic or dielectric structures that are used to manipulate light propagation in unusual ways compared to classical optical devices. These surfaces are capable of manipulating wavelength, polarization, and phase of incident waves. Hence, they can be used to realize the functionality of many classical optical devices as lenses, diffraction gratings, polarizers, and beam-splitters [16], [17]. Eventually, metasurfaces can provide combined conventional optical functions in addition to providing new functionalities as anomalous reflection governed by the generalized Snell's law of reflection, which is of particular interest in this work. A particularly interesting application of metasurfaces is the realization of flat focusing mirrors that are not attainable using conventional optics [18], [19]. To the best of our knowledge, this is the first study to consider utilizing IRSs for non-coherent VLC systems employing intensity-modulation/direct detection.

In this article, we propose an analytical framework to study the capabilities of both the adaptive metasurface and mirror array-based reflectors in focusing and aiming radiated power towards a specific detector. Towards this aim, we first derive the phase gradients to be applied to the metasurface array and the mirror array elements orientation needed to direct the incident power towards the detector center. Next, we derive expressions for the irradiance (power density) in the detector plane for both types of reflectors. After that, we derive simplified irradiance expressions under some relative locations and dimensions assumptions in addition corresponding to some practical special cases. Moreover, we introduce a new simple metric to judge the reflectors' relative performance from a received power perspective. Then, we quantify the received power gain compared with the power received from LoS. Finally, we study via simulation examples the impact of the number of reflecting elements, and detector location on the received power.

The rest of this article is organized as follows: firstly we provide a necessary background on light transportation in Section II. After that, we describe the adopted system model in Section III. Next, we derive the irradiance expressions for both setups in Sections IV and V. After that, we derive the irradiance at the detector center for several common practical special cases in Section VI. Then, we present analytic studies and insights in Section VII. Finally, we present several simulations in Section VIII followed by the conclusion in Section IX.

*Notation:* In this article, vectors are denoted by two capitalized bold letters such as $\mathbf{AB}$, where it starts from A and ends at B. $\mathbf{A}$ starts at origin and ends at A. $\mathbf{AB} = [\mathrm{AB}_x\ \mathrm{AB}_y\ \mathrm{AB}_z]^{\mathrm{T}} = \mathbf{B} - \mathbf{A}$, where $\mathrm{AB}_x$, $\mathrm{AB}_y$, and $\mathrm{AB}_z$ representing its $x$, $y$ and $z$ coordinates, respectively, and $(.)^{\mathrm{T}}$ represents the transpose operator. $\widehat{\mathbf{AB}}$ is the unit vector of $\mathbf{AB}$. We denote the unit vector representing the direction of a vector starting at point A and ending at point B by $\widehat{\mathbf{AB}}$. A$B$ represents a line segment between the points A and B. Moreover, we use $J(\frac{a,b}{c,d})$ to denote the determinant of the Jacobian matrix $\bar{J}(a, b, c, d)$, associated with the mapping of $c$ and $d$ variables into $a$ and $b$ variables, where $\bar{J} \triangleq [[\frac{\partial a}{\partial c}\ \frac{\partial b}{\partial c}]^T\ [\frac{\partial a}{\partial d}\ \frac{\partial b}{\partial d}]^T]$. Furthermore, we use $\|.\|_2$ to denote the $\ell_2$-norm, and $\mathbb{I}(C)$ as an indicator function where $\mathbb{I}(C) = 1$ if the condition $C$ is satisfied and $\mathbb{I}(C) = 0$, otherwise. As for symbols representing sets and matrices, the calligraphic and blackboard fonts are used, respectively. Finally, we use $|.|$ to represent the absolute value of a scalar and the Lebesgue measure of a set, while $\boldsymbol{e}_k$ denotes the $k$-th column in the $3 \times 3$ identity matrix.

## II. BACKGROUND

Throughout this work, we consider the non-coherent analysis of light propagation motivated by several reasons. The first reason is the random-phase nature of the radiation source. Also, the insignificance of interference and diffraction in the considered setups, where such effects need special arrangements for interference to appear for non-coherent sources [20, Ch. 7.3.4]. Finally, the mathematical intractability incurred in dealing with electromagnetic field expressions when considering metasurfaces and multi-element reflectors. In the following, we define light energy-based metrics and describe the light reflection patterns before delving into the analysis.

### A. FUNDAMENTAL RADIOMETRIC AND PHOTOMETRIC METRICS

In this section, we explain some fundamental metrics that describe light energy transportation in space. Radiometry studies the properties of radiation energy distribution in space, which is crucial for the communications service assessment of VLC systems. On the other hand, photometry is concerned with studying the human eye perception of light, which is crucial for the assessment and design of lighting systems [21].

Among the radiometric quantities, the following metrics are of particular relevance [22, Ch. 1.6], [23, Ch. 2.3], and [24, Ch. 13].

- **Radiant Flux** ($\Phi$) represents the rate of energy flow (radiated power) from/into a certain spatial region, and can be expressed as

$$\Phi = \int_{\lambda=380\text{nm}}^{740\text{nm}} P(\lambda) d\lambda \quad \text{(watt)}, \tag{1}$$

where $P(\lambda)$ represents the power spectral density of the radiated flux measured in watts per meter and $\lambda$ denotes the radiation wavelength.

- **Irradiance of a point on aVsurface** (**E**) is the amount of radiant flux incident on a unit area lying on that surface from all directions in the half-space above or below it. In other words, it represents areal radiant flux density (power density). It is worth noting that $E$ does not depend on the surface properties, where is defined as

$$E = \frac{d\Phi}{dA} \quad \left(\text{watt/m}^2\right), \tag{2}$$

where $dA$ is a differential area element containing the point at which irradiance is to be computed. Emittance follows the same definition of irradiance except that flux exits the surface of interest. Hence, the total incident flux on a given surface/detector represented by the set of points $\mathcal{Q}$ can be expressed as

$$\int_{\mathcal{Q}} E(\text{P}) dA_{\text{P}}, \tag{3}$$

where $dA_{\text{P}}$ represents a differential area element tangential to the considered surface at P.

- **Radiant intensity of a point source** (**I**) in a given direction is the amount of radiated flux by a point source per unit solid angle and is defined as,

$$I = \frac{d\Phi}{d\omega} \quad \text{(watt/steradian)}, \tag{4}$$

where $d\omega$ is a differential solid angle element around the desired measurement direction. $I$ represents also the angular radiant flux density. For a point isotropic source, $I = \frac{\Phi}{4\pi}$.

- **Radiance**(**L**) is defined as the amount of radiant flux per unit solid angle per unit area perpendicular to the direction of radiance measurement. Three constituents are needed to specify radiance, namely, a point, infinitesimal area containing this point, and a solid angle subtending the direction of measurement. Radiance can be attributed to any arbitrary point in space, with a possibly virtual area containing that point, nonetheless, computing radiance for a point on an extended source or a reflecting surface is of particular interest. Finally, it can be evaluated as

$$L = \frac{d^2\Phi}{dA_{\perp} d\omega} = \frac{d^2\Phi}{dA d\omega \cos(\theta_{\text{s}})} \triangleq \lim_{\Delta A \to 0, \Delta\omega \to 0} \frac{\Delta\Phi}{\Delta A \Delta\omega \cos(\theta_{\text{s}})}, \tag{5}$$

where $dA_{\perp}$ represents the projection of the differential area element containing the measurement point onto a plane that is orthogonal to the measurement direction, and $\theta_{\text{s}}$ is the angle between the normal to the area element and the direction around which the solid angle is defined as can be seen in Fig. 1. Equivalently, radiance can be defined by expressing its relationship with irradiance through the following integral,

$$E = \int_{\Omega} L \cos(\theta_{\text{s}}) d\omega, \tag{6}$$

where $\Omega$ is a hemispherical solid angle. It is worth noting that radiance is constant for all points lying on the ray representing direction of radiance measurement.

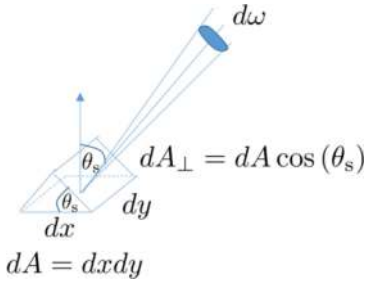


FIGURE 1. Radiance illustration.

As for the relevant photometric quantities, they follow very similar definitions to their radiometric counterparts with the exception that luminous flux is considered instead of radiant flux:

- **Luminous Flux** ($\Phi_{\text{v}}$) represents the optical power weighted by the eye sensitivity function ($V(\lambda)$), and can be expressed as

$$\Phi_{\text{v}} = \int_{\lambda=380\text{nm}}^{740\text{nm}} P(\lambda) V(\lambda) d\lambda \quad \text{lumens}, \tag{7}$$

where $V(\lambda)$ is the spectral efficacy function that specifies the relative response of human eye to different wavelengths. Illuminance, luminous intensity and luminance are the photometric counterparts of irradiance, radiant intensity, and radiance, respectively [22, Ch 2.2].

### B. LIGHT REFLECTION PATTERNS

Reflection response of a surface is highly determined by its constituting material and its geometric imperfections. Surface reflection response can be classified into: specular, diffuse, or glossy based on the roughness degree of the surface (determined by fluctuation in the height profile). Perfectly smooth surfaces act as mirrors and reflect light in a specular direction according to Snell's law of reflection while rough surfaces scatter incident light in all directions. Generally, surfaces have glossy nature where the reflected power consists of a specular component and a diffuse component. In this work, we are particularly interested in specular reflections.

## III. SYSTEM MODEL

In this work, we consider two different setups for intelligent reflecting surfaces in the context of VLC systems, namely,

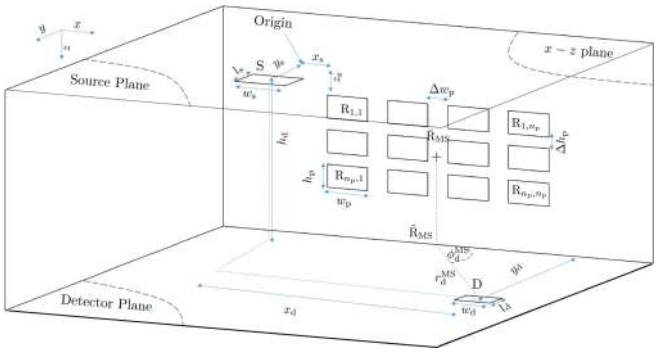


**FIGURE 2.** Metasurface-based IRS Model.

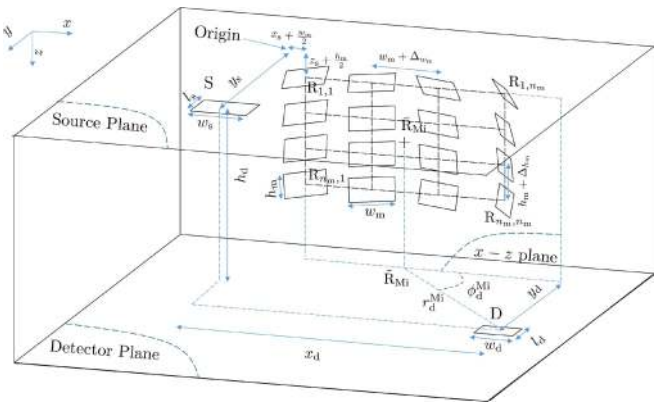


**FIGURE 3.** Mirror Array-based IRS Model.

intelligent metasurface reflector (IMR) and intelligent mirror array (IMA). In both setups, we assume a non-coherent LED transmitter [25, Ch. 2] that is horizontally-oriented and mounted to the room ceiling at a vertical clearance $h_d$ from the horizontal plane containing the receiver as depicted in Fig. 2[1] and Fig. 3. The $x$, $y$, and $z$ axes positive directions are oriented such that the $z$-axis is orthogonal to the ceiling and points towards the floor of the room, while the $y$-axis is normal to one of the walls and points at the source side, and the $x$-axis is oriented such that the three axes form a right-handed coordinate system. Moreover, we assume an extended planar source having uniform radiant emittance over its area $A_s = w_s l_s$ with $w_s$ and $l_s$ being the source span along the $x$-direction and $y$-direction, respectively. Each point on the transmitter aperture is assumed to have a generalized Lambertian radiation pattern with Lambertian order $m$. Hence, the radiance of a general point on the transmitter in a direction making an angle $\theta_s$ with the positive $z-$axis can be expressed based on [26, eq. (1)] as (for the proof see Appendix A)

$$L(\theta_s) = \frac{(m+1)p}{2\pi A_s} \cos^{m-1}(\theta_s), \tag{8}$$

where $m = -\ln(\cos(\phi_{1/2}))$, $\phi_{1/2}$ represents the half power beamwidth, and $p$ is the transmitter optical radiated power.

1. Parallel projection is used to plot all the figures hereafter. (i.e., parallel lines in the plot are physically parallel).

We denote the set of points representing the source aperture by $\mathcal{S}$.

Moreover, we assume a horizontally-oriented receiver (photo detector), where its center (D) is offset from the source center (S) by $x_d$ in the $x$-direction and by $y_d$ from the reflector in the y-direction. The detector extent along the $x$-direction is $w_d$, while its extent along the $y$-direction is $l_d$. Furthermore, the detection pattern is assumed to be Lambertian having a field-of-view of 90°, which can be realized using a hemispherical lens [27]. As for the reflectors, we detail their structure in the following subsections.

### A. INTELLIGENT METASURFACE REFLECTOR

In the first system setup, we consider an $n_p \times n_p$ array of identical rectangular optical metasurface patches, with patch width $w_p$ and patch height $h_p$ placed on a vertical surface with a normal vector parallel to the $y$-axis as depicted in Fig. 2. The edge-to-edge inter-patch separation distances are $\Delta_{h_p}$ and $\Delta_{w_p}$ along the $z$-axis and the $x$-axis, respectively. The reflector location is defined by a vertical offset $z_s$, with a minimum offset along the $x$-direction of $x_s$ and constant offset along the negative $y$-direction of $y_s$ for all the reflector points with all offsets being measured from the source center. Moreover, we assume that the phase discontinuity ($\Theta$) of each metasurface patch can be controlled independently of the other patches. It is further assumed that the phase gradient is kept constant over each metasurface patch (i.e., $\frac{\partial \Theta}{\partial x} = C^x_{k,\ell}$ and $\frac{\partial \Theta}{\partial z} = C^z_{k,\ell}\ \forall (x,z) \in \mathcal{R}^{MS}_{k,l}$, where $\mathcal{R}^{MS}_{k,l}\ \forall k,l$ represents the set of points lying on an arbitrarily chosen metasurface patch in the $k$-th row and $l$-th column of the reflector array).

### B. INTELLIGENT MIRROR ARRAY

In the second system, we consider an $n_m \times n_m$ two-dimensional array of identical rectangular mirrors whose centers lie in the $x-z$-plane as depicted in Fig. 3. We assume that the orientation of each mirror can be adjusted independently via two rotational degrees of freedom. In Fig. 4, we focus on the mirror whose center is positioned in the $k-$th row and $\ell-$th column of the array, and represent it mathematically by the set of points $\mathcal{R}^{Mi}_{k,\ell}$. The final mirror orientation is set via two successive clockwise rotations; the first is about the mirror local $z$-axis with an angle $\beta_{k,\ell}$ and the second is about the negative $x'-$axis (the mirror local negative $x-$axis after the first rotation).[2] At the mirrors default position ($\alpha_{k,\ell} = 0\ \forall k,\ell,\ \beta_{k,\ell} = 0\ \forall k,\ell$), they span $w_m$ and $h_m$ along the $x$-direction and the $z$-direction, respectively. Finally, the separation distances between adjacent mirrors centers are $w_m + \Delta_{w_m}$ and $h_m + \Delta_{h_m}$ along the $x$-axis and the $z$-axis, respectively.

In order to minimize the transmittance for both reflector types, the reflecting elements are chosen with much larger

2. It should be noticed from Fig. 4 that $x'$, $y'$, and $z'$ axes represent the $x$, $y$, and $z$ axes, respectively, after the first rotation around $z$, where $z$, $z'$ axes coincide. On the other hand, $x''$, $y''$, and $z''$ axes represent the $x$, $y$, $z$ axes, respectively, after the second rotation around $x'$, where $x'$, $x''$ axes coincide.

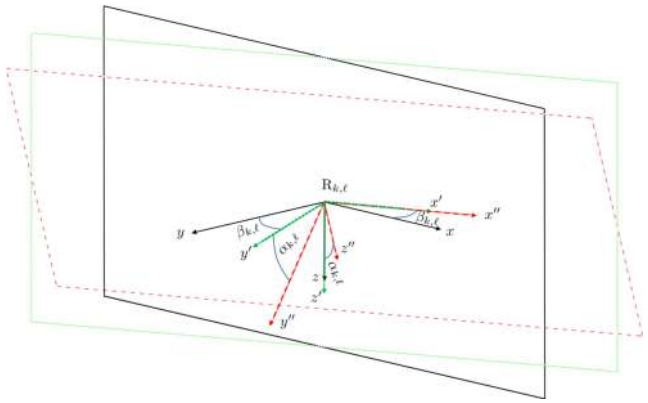

FIGURE 4. Rotational Degrees of Freedom of each Mirror.

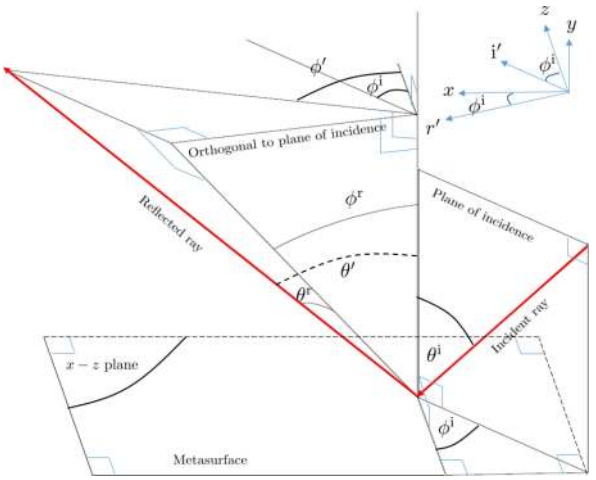


FIGURE 5. Generalized law of reflection.

thicknesses than the penetration depths of the employed metal. The skin depths for different metals are easily computable using the presented tables in [28, Ch. 2]. Unlike the adopted structure in [29], to avoid polarization sensitivity, both reflectors are built using neither birefringent nor dichroic materials.

Before delving into the derivation details presented in the following sections, it is important to highlight that the conducted analysis is based on radiometry, which stands on geometric optics grounds. The validity of this approach requires that the reflecting element's dimensions are much larger than the visible light wavelength [30, 15.2], [31, Ch. 2]. In this regard, we adopt a macroscopic model for the metasurface patches to abstract them as anomalous reflective rectangular blocks, which directs most of the incident power in a direction imposed by the generalized law of reflection depending on the incidence direction and the phase discontinuity profile of the metasurface [32].

## IV. IRRADIANCE PERFORMANCE OF INTELLIGENT METASURFACE REFLECTOR

In this section, we are interested in quantifying the potential gains of incorporating controllable metasurface-based IRs in VLC systems from a communication service perspective. Towards this end, we derive the irradiance generated at a certain point in the detector plane due to the first-order reflection from the metasurface-based reflector. Throughout this derivation, we assume

- the phase discontinuity function of each metasurface patch is tuned such that the incident ray from the source's center hitting the reflector's center reflects at the detector's center.
- the transmitter adjusts the symbol duration to avoid inter-symbol interference.
- the surfaces of the reflector elements are perfectly smooth to avoid the intricacies incurred in non-specular reflection analysis.
- the reflection coefficient magnitude does not depend on the direction of incidence.
- the controllable introduced phase-gradient on the metasurface is smooth for all directions lying on the surface.
- the data is carried on a monochromatic light to avoid reflection spectral dependencies.

### A. GENERALIZED LAW OF REFLECTION

Before proceeding with the irradiance derivation details, it is essential to highlight some properties of the generalized law of reflection (generalized Snell's law). In [33], the authors provided a relativistic description of the reflected ray direction with respect to the incident ray and the normal to the surface depending on the introduced phase-discontinuity on the metasurface. By applying their derived expressions while assuming the incident ray projection on the metasurface (lying in the $x-z$ plane) making an angle $\phi^i$ with the negative $z-$axis as shown in Fig. 5, the generalized law of reflection can be written as

$$\cos\left(\theta^{\mathrm{r}}\right)\sin\left(\phi^{\mathrm{r}}\right)=\frac{\lambda}{2\pi n_i}\frac{\partial\Theta}{\partial \mathrm{r}'}, \tag{9}$$

$$\sin\left(\theta^{\mathrm{r}}\right)-\sin\left(\theta^{\mathrm{i}}\right)=\frac{\lambda}{2\pi n_i}\frac{\partial\Theta}{\partial \mathrm{i}'}, \tag{10}$$

where $\theta^{\mathrm{r}}$ is the angle between the reflected ray and its projection on the plane orthogonal to the incidence plane and the metasurface, $\phi^{\mathrm{r}}$ is the angle between the normal to the metasurface and the reflected ray projection on the plane orthogonal to both the incidence plane and the metasurface, $\Theta$ represents the reflector phase discontinuity and $n_i$ is the refractive index of the medium of incidence and $\lambda$ represents the wavelength, $\theta^{\mathrm{i}}$ is the angle of incidence (angle between the incident ray and the normal to the metasurface), $i'$ and $r'$ represent the counter-clockwise rotated version of the $z-$ and $x-$ axes about the $y-$axis by an angle $\phi^i$, respectively, as can be seen in Fig. 5.

The previous relativistic formulation of the generalized Snell's law can be expressed in an absolute representation

as (for proof see Appendix B)

$$\sin(\theta')\sin(\phi') - \sin\left(\theta^{\mathrm{i}}\right)\sin\left(\phi^{\mathrm{i}}\right) = \frac{\lambda}{2\pi n_{\mathrm{i}}}\frac{\partial\Theta}{\partial x}, \quad (11)$$

$$\sin(\theta')\cos(\phi') - \sin\left(\theta^{\mathrm{i}}\right)\cos\left(\phi^{\mathrm{i}}\right) = \frac{\lambda}{2\pi n_{\mathrm{i}}}\frac{\partial\Theta}{\partial z}, \quad (12)$$

or, equivalently,

$$\theta^{\mathrm{i}} = \sin^{-1}\Bigg(\Bigg(\Bigg(\sin(\theta')\sin(\phi') - \frac{\lambda}{2\pi n_{\mathrm{i}}}\frac{\partial\Theta}{\partial x}\Bigg)^2 + \Bigg(\sin(\theta')\cos(\phi') - \frac{\lambda}{2\pi n_{\mathrm{i}}}\frac{\partial\Theta}{\partial z}\Bigg)^2\Bigg)^{\frac{1}{2}}\Bigg), \quad (13)$$

$$\phi^{\mathrm{i}} = \tan^{-1}\left(\frac{\sin(\theta')\sin(\phi') - \frac{\lambda}{2\pi n_{\mathrm{i}}}\frac{\partial\Theta}{\partial x}}{\sin(\theta')\cos(\phi') - \frac{\lambda}{2\pi n_{\mathrm{i}}}\frac{\partial\Theta}{\partial z}}\right) + \pi\mathbb{I}\left(\sin(\theta')\cos(\phi') - \frac{\lambda}{2\pi n_{\mathrm{i}}}\frac{\partial\Theta}{\partial z} < 0\right). \quad (14)$$

where $\theta'$ represents the angle between the normal to the metasurface and the reflected ray, and $\phi'$ denotes the angle between the projection of the reflected ray on the metasurface and a ray parallel to the $z$-axis lying in that plane. It can be noticed that when $\frac{\partial\Theta}{\partial x} = 0$ and $\frac{\partial\Theta}{\partial z} = 0$, (13), (14) represent the ordinary Snell's law of reflection.

A fundamental consequence of the generalized Snell's law is that it prohibits certain regions in the space of reflected rays directions. One can see clearly from (13) that there is no feasible $\theta^i$ corresponding to $\theta'$ and $\phi'$ values that violates

$$\left(\sin(\theta')\sin(\phi') - \frac{\lambda}{2\pi n_{\mathrm{i}}}\frac{\partial\Theta}{\partial x}\right)^2 + \left(\sin(\theta')\cos(\phi') - \frac{\lambda}{2\pi n_{\mathrm{i}}}\frac{\partial\Theta}{\partial z}\right)^2 \leq 1. \quad (15)$$

### B. IRRADIANCE DERIVATION

To lay the foundations for deriving the irradiance generated by the metasurface reflector, we introduce a thorough definition of the adopted geometry in the upcoming ray-tracing analysis.

In Fig. 6, we layout a geometric description of the main contributors to the reflection scene, and in Table 1 we provide their description.

In the following analysis, $\Gamma$, $\gamma$, and $\chi$ will take the values from the sets $\{\mathrm{I}_{\mathrm{R,P}}, \mathrm{I}_{\mathrm{R}_{k,\ell},\mathrm{P}}, \mathrm{S}\}$, $\{\mathrm{D}, \mathrm{P}\}$, and $\{\mathrm{R}, \mathrm{R}_{k,\ell}\}$, respectively.[3]

It can be deduced that the overall irradiance generated by the whole reflector array is the superposition of its individual elements irradiance contributions. Hence, we focus on the irradiance generated by the metasurface patch in the $k$-th row and the $\ell$-th column of the array, where row and column array indexing directions match the positive $z$- and $x-$axes, respectively, as indicated in Fig. 2. For each reflecting patch,

3. Unless otherwise stated, we use the presented angles definitions hereafter in the rest of the paper.

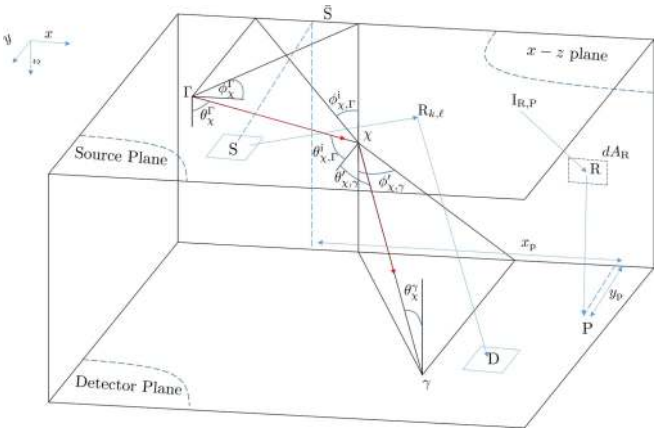


**FIGURE 6.** General ray tracing for metasurface-based IRS.

**TABLE 1.** Ray tracing parameters definitions.

| | |
|---|---|
| $\mathrm{S}$ | the source center |
| $\bar{\mathrm{S}}$ | the projection of S on the $x-z$ plane and represents the origin |
| $\mathrm{P}$ | the point of irradiance measurement in the detector plane ($z = h_{\mathrm{d}}$) |
| $\mathrm{I}_{\kappa,\mu}$ | a point in the source plane ($x-y$ plane) such that the incident ray originating at $\mathrm{I}_{\kappa,\mu}$, hitting the reflector at $\kappa$ is reflected towards $\mu$ in the detector plane. Equivalently, $\mathrm{I}_{\kappa,\mu}$ represents the pre-reflection image, in the source plane ($x-y$ plane), of $\mu$ when $\kappa$ is the reflection point. |
| $\mathrm{R}$ | an arbitrarily chosen point on the considered reflecting element |
| $\Gamma$ | a general point in the source plane |
| $\gamma$ | a general point in the detector plane |
| $\chi$ | a general point in the $x-z$ plane |
| $\theta^{\Gamma}_{\chi}$ | the angle between the positive $z-$axis and $\Gamma\chi$ |
| $\phi^{\Gamma}_{\chi}$ | the angle between the positive $x-$axis and the projection of $\Gamma\chi$ in the source plane |
| $\theta^{\gamma}_{\chi}$ | the angle between the negative $z-$axis and $\gamma\chi$ |
| $\theta^{\mathrm{i}}_{\chi,\Gamma}$ | the angle between $\Gamma\chi$ and the positive $y-$axis |
| $\phi^{\mathrm{i}}_{\chi,\Gamma}$ | the angle between the projection of $\Gamma\chi$ in the $x-z$ plane and the negative $z-$axis |
| $\theta'_{\chi,\gamma}$ | the angle between the positive $y-$axis and $\chi\gamma$ |
| $\phi'_{\chi,\gamma}$ | the angle between the projection of $\chi\gamma$ in the $x-z$ plane and the positive $z-$axis |

we study the irradiance contribution ($dE^{\mathrm{MS}}_{\mathrm{P}}$) of a differential area element ($dA_{\mathrm{R}}$), then exploit the superposition principle to find the overall performance. To find the $dE^{\mathrm{MS}}_{\mathrm{P}}$ at P due to $dA_{\mathrm{R}}$, we apply these steps:

- Find the tuned phase gradient, ($C^{x}_{k,\ell}$ and $C^{z}_{k,\ell}$), of the considered patch.
- Find the location of $\mathrm{I}_{\mathrm{R,P}}$ given $C^{x}_{k,\ell}$, $C^{z}_{k,\ell}$ and the locations of P and R.

We use $\theta^{\mathrm{S}}_{\mathrm{R}}$ and $\phi^{\mathrm{S}}_{\mathrm{R}}$ hereafter to specify the position of the reflector differential area element, and to describe all the required vectors to compute $dE^{\mathrm{MS}}_{\mathrm{P}}$. Consequently, the vector definitions of the key five points forming the ray tracing problem follow as

$$\mathbf{S} = \begin{bmatrix} 0 & y_{\mathrm{s}} & 0 \end{bmatrix}^{\mathrm{T}}, \quad (16)$$

$$\mathbf{D} = \begin{bmatrix} x_\mathrm{d} & y_\mathrm{d} & h_\mathrm{d} \end{bmatrix}^\mathrm{T}, \tag{17}$$

$$\mathbf{P} = \begin{bmatrix} x_\mathrm{p} & y_\mathrm{p} & h_\mathrm{d} \end{bmatrix}^\mathrm{T}, \tag{18}$$

$$\mathrm{R}_{\boldsymbol{k},\boldsymbol{\ell}} = \begin{bmatrix} x_\mathrm{s} + \frac{w_\mathrm{p}}{2} + (\ell-1)\left(w_\mathrm{p} + \Delta w_\mathrm{p}\right) \\ 0 \\ z_\mathrm{s} + \frac{h_\mathrm{p}}{2} + (k-1)\left(h_\mathrm{p} + \Delta h_\mathrm{p}\right) \end{bmatrix}, \tag{19}$$

$$\mathrm{R} = \begin{bmatrix} y_\mathrm{s}\cot\left(\phi_\mathrm{R}^\mathrm{S}\right) & 0 & y_\mathrm{s}\csc\left(\phi_\mathrm{R}^\mathrm{S}\right)\cot\left(\theta_\mathrm{R}^\mathrm{S}\right) \end{bmatrix}^\mathrm{T}. \tag{20}$$

The phase gradient over the metasurface patch can be expressed using (11) and (12) as

$$\begin{aligned} \left.\frac{\partial\Theta}{\partial \mathrm{R}_x}\right|_{\mathrm{R}\in\mathcal{R}_{k,\ell}^{\mathrm{MS}}} &= C_{k,\ell}^x = \frac{2\pi n_\mathrm{i}}{\lambda}\Big(\sin\left(\theta'_{\mathrm{R}_{k,\ell},\mathrm{D}}\right)\sin\left(\phi'_{\mathrm{R}_{k,\ell},\mathrm{D}}\right) \\ &\qquad - \sin\left(\theta^\mathrm{i}_{\mathrm{R}_{k,\ell},\mathrm{S}}\right)\sin\left(\phi^\mathrm{i}_{\mathrm{R}_{k,\ell},\mathrm{S}}\right)\Big) \\ &= \frac{2\pi n_\mathrm{i}}{\lambda}\left(\frac{\mathbf{R}_{k,\ell}\mathrm{D}^\mathrm{T}\boldsymbol{e}_1}{\|\mathbf{R}_{k,\ell}\mathrm{D}\|_2} - \frac{\mathrm{S}\mathbf{R}_{k,\ell}^\mathrm{T}\boldsymbol{e}_1}{\left\|\mathbf{R}_{k,\ell}\mathrm{S}\right\|_2}\right), \end{aligned} \tag{21}$$

$$\begin{aligned} \left.\frac{\partial\Theta}{\partial \mathrm{R}_z}\right|_{\mathrm{R}\in\mathcal{R}_{k,\ell}^{\mathrm{MS}}} &= C_{k,\ell}^z = \frac{2\pi n_\mathrm{i}}{\lambda}\Big(\sin\left(\theta'_{\mathrm{R}_{k,\ell},\mathrm{D}}\right)\cos\left(\phi'_{\mathrm{R}_{k,\ell},\mathrm{D}}\right) \\ &\qquad - \sin\left(\theta^\mathrm{i}_{\mathrm{R}_{k,\ell},\mathrm{S}}\right)\cos\left(\phi^\mathrm{i}_{\mathrm{R}_{k,\ell},\mathrm{S}}\right)\Big) \\ &= \frac{2\pi n_\mathrm{i}}{\lambda}\left(\frac{\mathbf{R}_{k,\ell}\mathrm{D}^\mathrm{T}\boldsymbol{e}_3}{\|\mathbf{R}_{k,\ell}\mathrm{D}\|_2} - \frac{\mathrm{S}\mathbf{R}_{k,\ell}^\mathrm{T}\boldsymbol{e}_3}{\left\|\mathbf{R}_{k,\ell}\mathrm{S}\right\|_2}\right). \end{aligned} \tag{22}$$

The second crucial step of this derivation is to find the location of $\mathrm{I}_{\mathrm{R,\,P}}$, which can be done by exploiting the generalized Snell's law, (13) and (14), to identify the corresponding incident ray to the reflected ray RP via $\theta_\mathrm{R}^\mathrm{i}$ and $\phi_\mathrm{R}^\mathrm{i}$ as[4]

$$\theta^\mathrm{i}_{\mathrm{R},\mathrm{I}_{\mathrm{R,P}}} = \sin^{-1}\left(\left(\left(\frac{x_\mathrm{p} - y_\mathrm{s}\cot\left(\phi_\mathrm{R}^\mathrm{S}\right)}{\ell_{\mathrm{RP}}} - c_{k,\ell}^x\right)^2 + \left(\frac{h_\mathrm{d} - y_\mathrm{s}\csc\left(\phi_\mathrm{R}^\mathrm{S}\right)\cot\left(\theta_\mathrm{R}^\mathrm{S}\right)}{\ell_{\mathrm{RP}}} - c_{k,\ell}^z\right)^2\right)^{\frac{1}{2}}\right), \tag{23}$$

$$\phi^\mathrm{i}_{\mathrm{R},\mathrm{I}_{\mathrm{R,P}}} = \tan^{-1}\left(\frac{\frac{x_\mathrm{p} - y_\mathrm{s}\cot\left(\phi_\mathrm{R}^\mathrm{S}\right)}{\ell_{\mathrm{RP}}} - c_{k,\ell}^x}{\frac{h_\mathrm{d} - y_\mathrm{s}\csc\left(\phi_\mathrm{R}^\mathrm{S}\right)\cot\left(\theta_\mathrm{R}^\mathrm{S}\right)}{\ell_{\mathrm{RP}}} - c_{k,\ell}^z}\right), \tag{24}$$

where $\ell_{\mathrm{R\,P}} = \|\mathbf{RP}\|_2$, $c_{k,\ell}^x = \frac{\lambda}{2\pi n_\mathrm{i}}C_{k,\ell}^x$ and $c_{k,\ell}^z = \frac{\lambda}{2\pi n_\mathrm{i}}C_{k,\ell}^z$. Consequently, $\mathrm{I}_{\mathrm{R,\,P}}$ can be expressed as

$$\mathrm{I}_{\mathrm{R,\,P}} = \begin{bmatrix} y_\mathrm{s}\cot\left(\phi_\mathrm{R}^\mathrm{S}\right) - y_\mathrm{s}\csc\left(\phi_\mathrm{R}^\mathrm{S}\right)\cot\left(\theta_\mathrm{R}^\mathrm{S}\right)\tan\left(\theta^\mathrm{i}_{\mathrm{R},\mathrm{I}_{\mathrm{R,P}}}\right) \\ y_\mathrm{s}\csc\left(\phi_\mathrm{R}^\mathrm{S}\right)\cot\left(\theta_\mathrm{R}^\mathrm{S}\right)\sec\left(\phi^\mathrm{i}_{\mathrm{R},\mathrm{I}_{\mathrm{R,P}}}\right)\cot\left(\theta^\mathrm{i}_{\mathrm{R},\mathrm{I}_{\mathrm{R,P}}}\right) \\ 0 \end{bmatrix}. \tag{25}$$

At this point, we express $dE_\mathrm{P}^{\mathrm{MS}}$ of $dA_\mathrm{R}$ using the differential form of (5) as

$$dE_\mathrm{p}^{\mathrm{MS}} = L_{\mathrm{P}\leftarrow\mathrm{R}}\cos\left(\theta_\mathrm{R}^\mathrm{P}\right)d\omega_{\mathrm{p}\leftarrow\mathrm{R}}, \tag{26}$$

4. It can be seen that the indicator term in (12) disappears in the $\phi_\mathrm{R}^i$ expression, as we do not consider backscattering scenarios in this work, i.e., the $z-$component of the incident ray is always positive.

where $L_{\mathrm{x}\leftarrow\mathrm{y}}$ denotes the radiance of the point y measured at the point x, and $d\omega_{\mathrm{P}\leftarrow\mathrm{R}}$ represents the differential solid angle subtended by $dA_\mathrm{R}$ measured at P. Using radiance invariance along the same ray [22, Ch. 1.6] and the differential solid angle definition, $dE_\mathrm{P}^{\mathrm{MS}}$ can be rewritten as

$$dE_\mathrm{p}^{\mathrm{MS}} = \rho_{\mathrm{MS}}L_{\mathrm{R}\leftarrow\mathrm{I_{R,P}}}\cos\left(\theta_\mathrm{R}^\mathrm{P}\right)dA_\mathrm{R}\cos\left(\theta'_{\mathrm{R,P}}\right)/\|\mathbf{RP}\|_2^2, \tag{27}$$

where $\rho_{\mathrm{MS}}$ represents the reflection efficiency. It is worth mentioning that $L_{\mathrm{R}\leftarrow\mathrm{I_{R,P}}} = 0$ if $\mathrm{I}_{\mathrm{R,\,P}}$ does not lie inside the source. We express $dA_\mathrm{R}$ in terms of $d\theta_\mathrm{R}^\mathrm{S}$ and $d\phi_\mathrm{R}^\mathrm{S}$ as

$$\begin{aligned} dA_\mathrm{R} &= \left|J\left(\frac{\mathrm{R}_x, \mathrm{R}_z}{\theta_\mathrm{R}^\mathrm{S}, \phi_\mathrm{R}^\mathrm{S}}\right)\right| d\theta_\mathrm{R}^\mathrm{S}d\phi_\mathrm{R}^\mathrm{S} \\ &= y_\mathrm{s}^2\csc^2\left(\theta_\mathrm{R}^\mathrm{S}\right)\left|\csc^3\left(\phi_\mathrm{R}^\mathrm{S}\right)\right| d\theta_\mathrm{R}^\mathrm{S}d\phi_\mathrm{R}^\mathrm{S}. \end{aligned} \tag{28}$$

From the setup geometry, it can be deduced easily that,

$$\cos\left(\theta_\mathrm{R}^\mathrm{P}\right) = \frac{h_\mathrm{d} - y_\mathrm{s}\csc\left(\phi_\mathrm{R}^\mathrm{S}\right)\cot\left(\theta_\mathrm{R}^\mathrm{S}\right)}{\ell_{\mathrm{RP}}\left(\phi_\mathrm{R}^\mathrm{S}, \theta_\mathrm{R}^\mathrm{S}\right)} \tag{29}$$

and

$$\cos\left(\theta'_{\mathrm{R,P}}\right) = \frac{y_\mathrm{p}}{\ell_{\mathrm{RP}}\left(\phi_\mathrm{R}^\mathrm{S}, \theta_\mathrm{R}^\mathrm{S}\right)}. \tag{30}$$

The radiance term $L_{\mathrm{R}\leftarrow\mathrm{I_{R,P}}}$ can be expressed as

$$\begin{aligned} L_{\mathrm{R}\leftarrow\mathrm{I_{R,P}}} &= \frac{\rho_{\mathrm{MS}}(m+1)p}{2\pi w_\mathrm{s}l_\mathrm{s}}\cos^{m-1}\left(\theta_\mathrm{R}^{\mathrm{I_{R,\,P}}}\right) \\ &\quad\times \mathbb{I}\left(\left|\mathrm{I}_{\mathrm{R,\,P}}^\mathrm{T}\boldsymbol{e}_1\right| \le \frac{w_\mathrm{s}}{2}, \left|\mathrm{I}_{\mathrm{R,\,P}}^\mathrm{T}\boldsymbol{e}_2\right| \le \frac{\ell_\mathrm{s}}{2}\right) \\ &\quad\times \mathbb{I}\Big(\left(\sin\left(\theta'_{\mathrm{R,P}}\right)\sin\left(\phi'_{\mathrm{R,I_{R,P}}}\right) - c_{k,\ell}^x\right)^2 \\ &\qquad + \left(\sin\left(\theta'_{\mathrm{R,P}}\right)\cos\left(\phi'_{\mathrm{R,I_{R,P}}}\right) - c_{k,\ell}^z\right)^2 \le 1\Big), \end{aligned} \tag{31}$$

where

$$\cos\left(\theta_\mathrm{R}^{\mathrm{I_{R,\,P}}}\right) = \frac{\csc\left(\phi_\mathrm{R}^\mathrm{S}\right)\cot\left(\theta_\mathrm{R}^\mathrm{S}\right)}{\sqrt{\tan^2\left(\theta^\mathrm{i}_{\mathrm{R},\mathrm{I}_{\mathrm{R,P}}}\right) + \left(\sec\left(\phi^\mathrm{i}_{\mathrm{R},\mathrm{I}_{\mathrm{R,P}}}\right)\cot\left(\theta^\mathrm{i}_{\mathrm{R},\mathrm{I}_{\mathrm{R,P}}}\right)\right)^2}}, \tag{32}$$

and we used the first indicator term to ensure that $\mathrm{I}_{\mathrm{R,\,P}}$ does not contribute to the computed irradiance if it lies outside the source boundaries. We use the second indicator to ensure a correct angle of incidence that can result in a reflection from R to P based on the set phase gradient. Finally, we evaluate the total irradiance at P due to the first-order reflections by integrating over the considered metasurface patch area and summing up all patches contributions as

$$\begin{aligned} E_\mathrm{P}^{\mathrm{MS}} &= \frac{\rho_{\mathrm{MS}}(m+1)p}{2\pi w_\mathrm{s}l_\mathrm{s}}\sum_{k=1}^{n_\mathrm{p}}\sum_{\ell=1}^{n_\mathrm{p}}\int_{\phi_{k,\ell}^{\min}}^{\phi_{k,\ell}^{\max}}\int_{\theta_{k,\ell}^{\min}}^{\theta_{k,\ell}^{\max}}\cos^{m-1}\left(\theta_\mathrm{R}^{\mathrm{I_{R,\,P}}}\right) \\ &\quad\times \mathbb{I}\left(\left|\boldsymbol{e}_1^\mathrm{T}\mathrm{I}_{\mathrm{R,\,P}}\right| \le \frac{w_\mathrm{s}}{2}, \left|\boldsymbol{e}_2^\mathrm{T}\mathrm{I}_{\mathrm{R,\,P}}\right| \le \frac{\ell_\mathrm{s}}{2}\right) \end{aligned}$$

$$\times \mathbb{I}\left(\left(\frac{y_s\cot\left(\phi_R^S\right)-x_p}{\ell_{RP}}-c_{k,\ell}^x\right)^2+\left(\frac{h_d-y_s\csc\left(\phi_R^S\right)\cot\left(\theta_R^S\right)}{\ell_{RP}}-c_{k,\ell}^z\right)^2\le 1\right)$$
$$\times \frac{y_p\left(h_d-y_s\csc\left(\phi_R^S\right)\cot\left(\theta_R^S\right)\right)}{\ell_{RP}^4\left(\phi_R^S,\theta_R^S\right)}y_s^2\csc^2\left(\theta_R^S\right)$$
$$\times \left|\csc^3\left(\phi_R^S\right)\right|d\theta_R^S d\phi_R^S, \tag{33}$$

where

$$\phi_{k,\ell}^{\min}=\tan^{-1}\left(\frac{y_s}{x_s+(\ell-1)\left(w_p+\Delta w_p\right)}\right), \tag{34}$$

$$\phi_{k,\ell}^{\max}=\tan^{-1}\left(\frac{y_s}{x_s+w_p+(\ell-1)\left(w_p+\Delta w_p\right)}\right), \tag{35}$$

$$\theta_{k,\ell}^{\min}=\max\left(\tan^{-1}\left(\frac{y_s\csc\left(\phi_R^S\right)}{z_s+h_p+(k-1)\left(h_p+\Delta h_p\right)}\right),0\right), \tag{36}$$

$$\theta_{k,\ell}^{\max}=\min\left(\tan^{-1}\left(\frac{y_s\csc\left(\phi_R^S\right)}{z_s+(k-1)\left(h_p+\Delta h_p\right)}\right),\tan^{-1}\left(\frac{y_s\csc\left(\phi_R^S\right)}{h_d}\right)\right). \tag{37}$$

One can notice that $\phi_{k,\ell}^{\min}$ and $\phi_{k,\ell}^{\max}$ defines the horizontal boundaries, and $\theta_{k,\ell}^{\min}$ and $\theta_{k,\ell}^{\max}$ define the vertical boundaries of the metasurface patch in the $k$-th row and $\ell$-th column. The values of $\theta_{k,\ell}^{\min}$ and $\theta_{k,\ell}^{\max}$ are set to ensure that only the active portion of the metasurface patch (the part which is below the source and above the detector surface) contributes to the computed irradiance.

## V. IRRADIANCE PERFORMANCE OF INTELLIGENT MIRROR ARRAY REFLECTOR

In this section, we aim at assessing the advantages provided by mirror array reflectors when employed within VLC systems by analyzing their power focusing capability. To this end, we derive an expression for the irradiance at a general point in the detector plane whilst considering only first-order reflections from the mirrors array. We assume that the two rotational degrees of freedom of the reflecting element located at the $k$-th row and the $\ell$-th column in the array, namely, $\alpha_{k,\ell}$ and $\beta_{k,\ell}$ range within $[-\pi/2,\pi/2]$. The reflecting elements orientation represented by $\alpha_{k,\ell}$ and $\beta_{k,\ell}$ $\forall k,\ell$ is set such that the incident ray from the source center on the reflecting element center hits the detector center. In addition, we follow similar assumptions to those of the intelligent metasurface reflector regarding light rays path difference delays, surface smoothness, perfect conductance (negligible effect of incidence angle on the magnitude of reflection coefficient) besides the monochromaticity of the light carrying the data stream.

Similar to the metasurface case, we analyze the mirror centered at the $k$-th row and $\ell$-th column of the array, then sum up all the contributions for all $k,\ell$. Firstly, we define a local Cartesian coordinate system having its origin at the mirror center $\mathrm{R}_{k,\ell}$ and its axes orientation as shown in Fig. 3. Consequently, the main points vector definitions are given as[5]

$$\mathbf{S}=\begin{bmatrix}-\left(x_s+\frac{w_m}{2}+(\ell-1)(w_m+\Delta w_m)\right)\\ y_s\\ -\left(z_s+\frac{h_m}{2}+(k-1)(h_m+\Delta h_m)\right)\end{bmatrix}, \tag{38}$$

$$\mathbf{D}=\begin{bmatrix}x_d-\left(x_s+\frac{w_m}{2}+(\ell-1)(w_m+\Delta w_m)\right)\\ y_d\\ h_d-\left(z_s+\frac{h_m}{2}+(k-1)(h_m+\Delta h_m)\right)\end{bmatrix}, \tag{39}$$

$$\mathbf{P}=\begin{bmatrix}x_p-\left(x_s+\frac{w_m}{2}+(\ell-1)(w_m+\Delta w_m)\right)\\ y_p\\ h_d-\left(z_s+\frac{h_m}{2}+(k-1)(h_m+\Delta h_m)\right)\end{bmatrix}, \tag{40}$$

where $x_p$, $y_p$ represent the $x-$ and $y-$ coordinates of P as measured from $\bar{\mathrm{S}}$.

Before proceeding further, the mirror orientation is determined by finding a unit vector normal to its surface, namely, $\widehat{\mathrm{N}}_{k,\ell}$. In this setup, the mirror orientation is adjusted such that $\widehat{\mathbf{SR}_{k,\ell}}$ represents the corresponding incidence direction for the reflection direction $\widehat{\mathrm{R}_{k,\ell}\mathbf{D}}$. Hence, by the virtue of Snell's law of reflection, we solve [23, eq. (2.24)] for the normal vector direction and express $\widehat{\mathrm{N}}_{k,\ell}$ as $(\widehat{\mathrm{R}_{k,\ell}\mathbf{S}}+\widehat{\mathrm{R}_{k,\ell}\mathbf{D}})/\sqrt{2+2\widehat{\mathrm{R}_{k,\ell}\mathbf{S}}^{\mathrm{T}}\widehat{\mathrm{R}_{k,\ell}\mathbf{D}}}$. The angles defining the considered mirror orientation can be expressed in terms of $\widehat{\mathrm{N}}_{k,\ell}$ as

$$\beta_{k,\ell}=\sin^{-1}\left(\widehat{\mathrm{N}}_{k,\ell}^{\mathrm{T}}\boldsymbol{e}_3\right) \tag{41}$$

and

$$\alpha_{k,\ell}=\sin^{-1}\left(\widehat{\mathrm{N}}_{k,\ell}^{\mathrm{T}}\boldsymbol{e}_1/\cos\left(\beta_{k,\ell}\right)\right). \tag{42}$$

We define another Cartesian coordinate system that is local to the considered mirror having $\mathrm{R}_{k,\ell}$ as the origin. The axes of the new system are $x''$, $y''$, and $z''$ represent the rotated versions of the original $x$, $y$, and $z$ axes, respectively, as can be seen in Fig. 4 and Fig. 7. The switching between the two coordinate systems can be expressed as follows [34, Ch. 6]

$$\begin{bmatrix}A_{x''} & A_{y''} & A_{z''}\end{bmatrix}^{\mathrm{T}}=\left(\mathbb{R}_{k,\ell}^{x'}\mathbb{R}_{k,\ell}^{z}\right)^{\mathrm{T}}\begin{bmatrix}A_x & A_y & A_z\end{bmatrix}^{\mathrm{T}}, \tag{43}$$

where $A_{x''}, A_{y''}$, and $A_{z''}$ are the coordinates of an arbitrarily chosen point $A$ with respect to the axes $x''$, $y''$, and $z''$, respectively, while its coordinates with respect to the axes $x, y$, and $z$ are $A_x, A_y$ and $A_z$, respectively, $\mathbb{R}_{k,\ell}^{x'}$ represents a counter-clockwise rotation matrix about the $x'$ axis with

5. The physical definitions of the six main points in the ray tracing problem (S, $\mathrm{I}_{\mathrm{R,\,P}}$,D, P, R, and $\mathrm{R}_{k,\ell}$) in this section are identical to their counterparts in Section IV. They are only represented with respect to different coordinate systems.

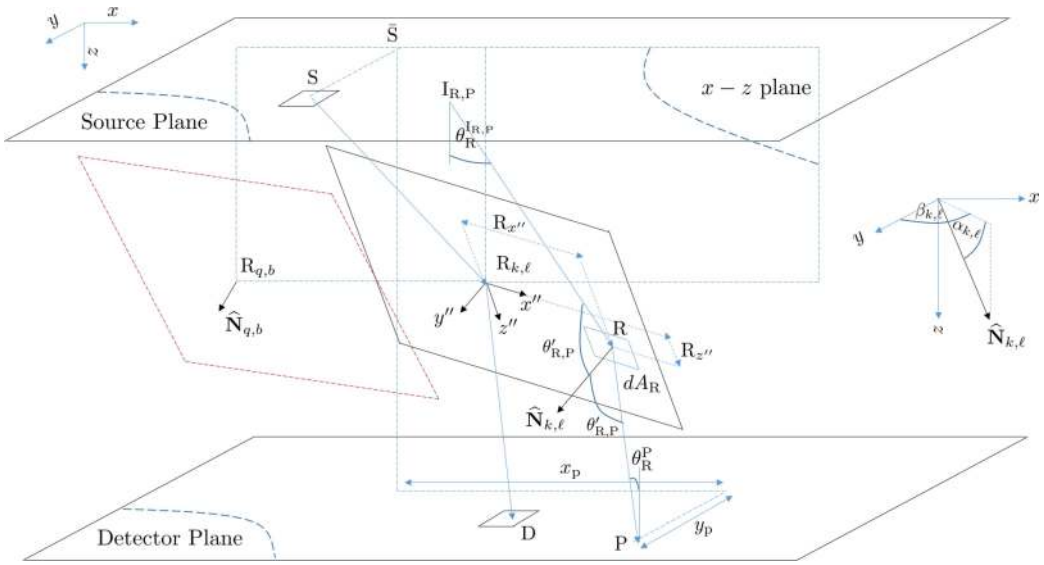


**FIGURE 7.** Ray tracing for mirror array-based IRS.

angle $\alpha_{k,\ell}$ and expressed as in (44) appearing at the bottom of the page.

$\mathbb{R}^{z}_{k,\ell}$ represents a clockwise rotation matrix about the $z$ axis with angle $\beta_{k,\ell}$ and is expressed as

$$\mathbb{R}^{z}_{k,\ell} = \begin{bmatrix} \cos(\beta_{k,\ell}) & \sin(\beta_{k,\ell}) & 0 \\ -\sin(\beta_{k,\ell}) & \cos(\beta_{k,\ell}) & 0 \\ 0 & 0 & 1 \end{bmatrix}. \tag{45}$$

At this stage, we divide the considered mirror into infinitesimally small differential area elements and add up their irradiance contribution to find the mirror total irradiance. We focus on studying the irradiance contribution $dE_{\mathrm{P}}^{\mathrm{Mi}}$ of the differential area element $dA_{\mathrm{R}}$ lying on the considered mirror at R as shown in Fig. 3. We define the location of R using (43)-(45), as $\mathbf{R} = \mathbb{R}^{x'}_{k,\ell}\mathbb{R}^{z}_{k,\ell}\begin{bmatrix}\mathrm{R}_{x''} & 0 & \mathrm{R}_{z''}\end{bmatrix}^{\mathrm{T}}$, where $\mathrm{R}_{x''}$ and $\mathrm{R}_{z''}$, respectively, represent the $x$ and $z$ coordinates of the point R with respect to the rotated coordinate system (represented by the $x''$, $y''$, and $z''$ axes).

In similarity to (27), $dE_{\mathrm{p}}^{\mathrm{Mi}}$ is expressed as

$$dE_{\mathrm{p}}^{\mathrm{Mi}} = \rho_{\mathrm{Mi}} L_{\mathrm{R}\leftarrow\mathrm{I_{R,P}}} \cos\left(\theta_{\mathrm{R}}^{\mathrm{P}}\right) d\mathrm{R}_{x''} d\mathrm{R}_{z''} \cos\left(\theta'_{\mathrm{R,P}}\right) / \|\mathbf{RP}\|_2^2, \tag{46}$$

where $\rho_{\mathrm{Mi}}$ represents the mirror reflection efficiency, $\theta'_{\mathrm{R,P}}$ denotes the angle between $\widehat{\mathrm{N}}_{k,\ell}$ and $\mathbf{RP}$, $\cos(\theta_{\mathrm{R}}^{\mathrm{P}}) = \boldsymbol{e}_3^{\mathrm{T}}\widehat{\mathbf{PR}}$, and $\cos(\theta'_{\mathrm{R,P}}) = \widehat{\mathrm{N}}_{k,\ell}^{\mathrm{T}}\widehat{\mathbf{RP}}$.

To find the location of $\mathrm{I_{R,P}}$, we first express the incidence direction $\widehat{\mathrm{I_{R,P}R}}$ corresponding to the reflection direction $\widehat{\mathbf{RP}}$ using [23, eq. (2.24)] as $\widehat{\mathrm{I_{R,P}R}} = -(2(\widehat{\mathrm{N}}_{k,\ell}^{\mathrm{T}}\widehat{\mathbf{RP}})\widehat{\mathrm{N}}_{k,\ell} - \widehat{\mathrm{RP}})$. The position vector describing a point $\tilde{\mathrm{I}}_{\mathrm{R,P}}$ lying on the ray starting from R and pointing towards $\mathrm{I_{R,P}}$ can be expressed as $\tilde{\mathrm{I}}_{\mathrm{R,P}} = \mathrm{R} + t\widehat{\mathrm{RI}}_{\mathrm{R,P}}$, $t \geq 0$. It can be deduced easily that $\tilde{\mathrm{I}}_{\mathrm{R,P}}$ coincides with $\mathrm{I_{R,P}}$ when the $z$ component of $\tilde{\mathrm{I}}_{\mathrm{R,P}}$ equals its counterpart of $\mathbf{S}$. Hence, $\mathrm{I_{R,P}}$ can be expressed as

$$\mathbf{I}_{\mathrm{R,P}} = \begin{bmatrix} \boldsymbol{e}_1^{\mathrm{T}}\left(\mathbf{R} + \frac{\boldsymbol{e}_3^{\mathrm{T}}\mathbf{RS}}{\boldsymbol{e}_3^{\mathrm{T}}\widehat{\mathrm{RI}}_{\mathrm{R,P}}}\widehat{\mathrm{RI}}_{\mathrm{R,P}}\right) \\ \boldsymbol{e}_2^{\mathrm{T}}\left(\mathbf{R} + \frac{\boldsymbol{e}_3^{\mathrm{T}}\mathbf{RS}}{\boldsymbol{e}_3^{\mathrm{T}}\widehat{\mathrm{RI}}_{\mathrm{R,P}}}\widehat{\mathrm{RI}}_{\mathrm{R,P}}\right) \\ \boldsymbol{e}_3^{\mathrm{T}}\mathbf{S} \end{bmatrix}. \tag{47}$$

Finally, to evaluate $dE_{\mathrm{p}}^{\mathrm{Mi}}$ from (46), we need to check whether the path between R and P and that between R and $\mathrm{I_{R,P}}$ are blocked by any other mirror in the array. We consider another arbitrarily chosen mirror, represented by $\mathcal{R}_{q,b}^{\mathrm{Mi}}$, (not containing the differential area element being studied) indexed by row and column indices $q$ and $b$, respectively. Then, we study whether RP intersects $\mathcal{R}_{q,b}^{\mathrm{Mi}}$ or not. On the one hand, the vector representation of a point U on the line segment RP can be expressed as $\mathbf{U}(\gamma) = \gamma\mathbf{R} + (1-\gamma)\mathbf{P}$, $\gamma \in [0,1]$. On the other hand, a general point V lying in the plane containing $\mathcal{R}_{q,b}^{\mathrm{Mi}}$ should satisfy

$$\widehat{\mathrm{N}}_{q,b}^{\mathrm{T}}\mathbf{V} = \widehat{\mathrm{N}}_{q,b}^{\mathrm{T}}\mathbf{R}_{q,b} = \widehat{\mathrm{N}}_{q,b}^{\mathrm{T}}\begin{bmatrix}(b-\ell)(w_{\mathrm{m}}+\Delta w_{\mathrm{m}}) \\ 0 \\ (q-k)(h_{\mathrm{m}}+\Delta h_{\mathrm{m}})\end{bmatrix}, \tag{48}$$

where $\widehat{\mathrm{N}}_{q,b}$ represents a unit vector normal to $\mathcal{R}_{q,b}^{\mathrm{Mi}}$. At the intersection of RP and $\mathcal{R}_{q,b}^{\mathrm{Mi}}$, $\mathrm{U}_{q,b} \triangleq \mathbf{U}(\gamma_{q,b,1}) = \mathbf{V}$.

$$\mathbb{R}^{x'}_{k,\ell} = \begin{bmatrix} \cos^2(\beta_{k,\ell})(1-\cos(\alpha_{k,\ell})) + \cos(\alpha_{k,\ell}) & -\cos(\beta_{k,\ell})\sin(\beta_{k,\ell})(1-\cos(\alpha_{k,\ell})) & -\sin(\beta_{k,\ell})\sin(\alpha_{k,\ell}) \\ -\cos(\beta_{k,\ell})\sin(\beta_{k,\ell})(1-\cos(\alpha_{k,\ell})) & \sin^2(\beta_{k,\ell})(1-\cos(\alpha_{k,\ell})) + \cos(\alpha_{k,\ell}) & -\cos(\beta_{k,\ell})\sin(\alpha_{k,\ell}) \\ \sin(\beta_{k,\ell})\sin(\alpha_{k,\ell}) & \cos(\beta_{k,\ell})\sin(\alpha_{k,\ell}) & \cos(\alpha_{k,\ell}) \end{bmatrix} \tag{44}$$

Hence, $\gamma_{q,b,1}$ can be expressed as $\widehat{\mathrm{N}}_{q,b}^{\mathrm{T}}\mathbf{PR}_{q,b}/(\widehat{\mathrm{N}}_{q,b}^{\mathrm{T}}\mathbf{PR})$, which reduces to

$$\gamma_{q,b,1} = \widehat{\mathrm{N}}_{q,b}^{\mathrm{T}}\left(\begin{bmatrix}(b-\ell)(w_{\mathrm{m}}+\Delta w_{\mathrm{m}})\\ 0\\ (q-k)(h_{\mathrm{m}}+\Delta h_{\mathrm{m}})\end{bmatrix} - \mathbf{P}\right)\Big/\left(\widehat{\mathrm{N}}_{q,b}^{\mathrm{T}}\mathbf{PR}\right). \tag{49}$$

It is clear that $\gamma_{q,b,1} > 1$, or $\gamma_{q,b,1} < 0$ is sufficient to declare that $\mathcal{R}_{q,b}^{\mathrm{Mi}}$ does not block the path RP. To assert the existence of $\mathrm{U}_{q,b}$ within $\mathcal{R}_{q,b}^{\mathrm{Mi}}$ boundaries, we compute the vector representation of $\mathrm{U}_{q,b}$ with respect to the local rotated axes of the $\mathcal{R}_{q,b}^{\mathrm{Mi}}$ as $\mathrm{U}_{q,b,1}^{\mathrm{r}} = (\mathbb{R}_{k,\ell}^{x'}\mathbb{R}_{k,\ell}^{z})^{\mathrm{T}}\mathrm{R}_{q,b}\mathbf{U}_{q,b,1}$. In a similar way to the definitions of $\gamma_{q,b,1}$, $\mathrm{U}_{q,b,1}$, and $\mathrm{U}_{q,b,1}^{\mathrm{r}}$, we define $\gamma_{q,b,2}$, $\mathrm{U}_{q,b,2}$, and $\mathrm{U}_{q,b,2}^{\mathrm{r}}$ to study the potential blockage of the path between R and $\mathrm{I}_{\mathrm{R,P}}$. Hence, the blockage event occurs if $|\boldsymbol{e}_1^{\mathrm{T}}\mathrm{U}_{q,b,1}^{\mathrm{r}}| \le w_{\mathrm{m}}/2$ and $|\boldsymbol{e}_3^{\mathrm{T}}\mathrm{U}_{q,b,1}^{\mathrm{r}}| \le h_{\mathrm{m}}/2$, or $|\boldsymbol{e}_1^{\mathrm{T}}\mathrm{U}_{q,b,2}^{\mathrm{r}}| \le w_{\mathrm{m}}/2$ and $|\boldsymbol{e}_3^{\mathrm{T}}\mathrm{U}_{q,b,2}^{\mathrm{r}}| \le h_{\mathrm{m}}/2$. Consequently, the radiance term $L_{\mathrm{R}\leftarrow\mathrm{I_{R,P}}}$ can be expressed as

$$\begin{aligned}
&L_{\mathrm{R}\leftarrow\mathrm{I_{R,P}}}\\
&= \rho_{\mathrm{Mi}}\frac{(m+1)}{2\pi w_{\mathrm{s}}l_{\mathrm{s}}}p\cos^{m-1}\left(\theta_{\mathrm{R}}^{\mathrm{I_{R,P}}}\right)\\
&\quad\times\left(1-\prod_{(q,b)\neq(k,\ell)}\mathbb{I}\left(\left|\boldsymbol{e}_1^{\mathrm{T}}\mathrm{U}_{q,b,1}^{\mathrm{r}}\right|\le\frac{w_{\mathrm{m}}}{2},\left|\boldsymbol{e}_3^{\mathrm{T}}\mathrm{U}_{q,b,1}^{\mathrm{r}}\right|\le\frac{h_{\mathrm{m}}}{2}\right)\right.\\
&\qquad\left.\times\,\mathbb{I}\big(0\le\gamma_{q,b,1}\le 1\big)\right)\\
&\quad\times\mathbb{I}\left(\left|\boldsymbol{e}_1^{\mathrm{T}}\mathbf{SI}_{\mathrm{R,P}}\right|\le\frac{w_{\mathrm{s}}}{2},\left|\boldsymbol{e}_2^{\mathrm{T}}\mathbf{SI}_{\mathrm{R,P}}\right|\le\frac{h_{\mathrm{s}}}{2}\right)\\
&\quad\times\mathbb{I}\left(\boldsymbol{e}_3^{\mathrm{T}}\mathbf{S}\le\boldsymbol{e}_3^{\mathrm{T}}\left(\mathbb{R}_{k,\ell}^{x'}\mathbb{R}_{k,\ell}^{z}\right)\begin{bmatrix}\mathrm{R}_{x''} & 0 & \mathrm{R}_{z''}\end{bmatrix}^{\mathrm{T}}\le\boldsymbol{e}_3^{\mathrm{T}}\mathbf{P}\right),
\end{aligned}\tag{50}$$

where $\theta_{\mathrm{R}}^{\mathrm{I_{R,P}}}$ denotes the angle between $\mathrm{I_{R,P}R}$ and the positive $z$-axis, and $\cos(\theta_{\mathrm{R}}^{\mathrm{I_{R,P}}}) = \boldsymbol{e}_3^{\mathrm{T}}\widehat{\mathrm{I_{R,P}R}}$.

Finally, we can express $E_{\mathrm{P}}^{\mathrm{Mi}}$ on a horizontal surface with an infinitesimal area around P as in (51) appearing at the bottom of the page, where $T_1$ nullifies the contributions of reflector points not lying vertically between S and P, while $T_2$ voids the effect of reflector portions hit by rays originating outside the source boundaries. The last term $T_3$ ensures that self blocked rays are not counted.

## VI. IRRADIANCE PERFORMANCE FOR DIFFERENT SPECIAL CASES

In this section, we derive simplified irradiance expressions based on different geometrical assumptions. Firstly, neglecting the inter-element blockage effect for the mirror array reflector, we can express the irradiance at the detector center for both reflector types as

$$\begin{aligned}
E_{\mathrm{D}}^{t} = \rho_t\sum_{k=1}^{n_t}\sum_{\ell=1}^{n_t}\iint_{\mathcal{R}_{k,\ell}^{t}}&\frac{(m+1)p\cos^{m-1}\left(\theta_{\mathrm{R}}^{\mathrm{I}_{\mathrm{R,D}}^{t}}\right)}{2\pi A_{\mathrm{s}}\|\mathbf{RD}\|_2^2}\\
&\times\cos\big(\theta_{\mathrm{R}}^{\mathrm{D}}\big)\cos\big(\theta_{\mathrm{R,D}}^{t}\big)\mathbb{I}\big(\mathrm{I}_{\mathrm{R,D}}^{t}\in\mathcal{S}\big)dA_{\mathrm{R}}^{t},
\end{aligned}\tag{52}$$

where we use the $t$ subscript/superscript, hereafter, to associate terms with the considered reflector type. Hence, $t \in \{\mathrm{MS,Mi}\}$, represents metasurface, mirror array reflectors, respectively, for all the variable definitions except for $n_t, w_t, h_t$, for which $t \in \{\mathrm{p,m}\}$. Finally, $\theta_{\mathrm{R,D}}^{t}$, represents $\theta_{\mathrm{R,D}}'$, $\mathrm{I}_{\mathrm{R},\gamma}^{t}$ represents $\mathrm{I}_{\mathrm{R},\gamma}$ with the considered reflector represented by $t$. Then, we assume, hereafter, a small detector regime (the detector largest dimension is much smaller than the minimum distance between a point on the reflector and a point on the detector). Hence, the irradiance variations over the detector surface are negligible and we can focus on the irradiance at the detector center. In the following subsections, we consider two major special cases, namely, the point source case and the large source small reflector case.

### A. POINT SOURCE CASE

In this case, the source dimensions are considered negligible compared with the distances between the reflector points and the source. Thus, any observation point on the reflector surface will perceive all source points with the same location, which allows us to deal with the source as a point.

$$\begin{aligned}
E_{\mathrm{P}}^{\mathrm{Mi}} = \frac{(m+1)p}{2\pi w_{\mathrm{s}}l_{\mathrm{s}}}\sum_{k=1}^{n_{\mathrm{m}}}\sum_{\ell=1}^{n_{\mathrm{m}}}\int_{-h_{\mathrm{m}}/2}^{h_{\mathrm{m}}/2}\int_{-w_{\mathrm{m}}/2}^{w_{\mathrm{m}}/2}&\left(\boldsymbol{e}_3^{\mathrm{T}}\widehat{\mathrm{I_{R,P}R}}\right)^{m-1}\frac{\left(\boldsymbol{e}_3^{\mathrm{T}}\widehat{\mathbf{RP}}\right)\left(\widehat{\mathbf{N}}_{k,\ell}^{\mathrm{T}}\widehat{\mathbf{RP}}\right)}{\|\mathbf{RP}\|_2^2}\underbrace{\mathbb{I}\left(\boldsymbol{e}_3^{\mathrm{T}}\mathbf{S}\le\boldsymbol{e}_3^{\mathrm{T}}\left(\mathbb{R}_{k,\ell}^{x'}\mathbb{R}_{k,\ell}^{z}\right)\begin{bmatrix}\mathrm{R}_{x''}\\0\\\mathrm{R}_{z''}\end{bmatrix}\le\boldsymbol{e}_3^{\mathrm{T}}\mathbf{P}\right)}_{T_1}\\
\times\underbrace{\mathbb{I}\left(\left|\boldsymbol{e}_1^{\mathrm{T}}\mathbf{SI}_{\mathrm{R,P}}\right|\le\frac{w_{\mathrm{s}}}{2},\left|\boldsymbol{e}_2^{\mathrm{T}}\mathbf{SI}_{\mathrm{R,P}}\right|\le\frac{h_{\mathrm{s}}}{2}\right)}_{T_2}&\underbrace{\prod_{j=1}^{2}\left(1-\prod_{\substack{(q,\,b)\\\neq\\(k,\,\ell)}}\mathbb{I}\left(\left|\boldsymbol{e}_1^{\mathrm{T}}\mathrm{U}_{q,b,j}^{\mathrm{r}}\right|\le\frac{w_{\mathrm{m}}}{2},\left|\boldsymbol{e}_3^{\mathrm{T}}\mathrm{U}_{q,b,j}^{\mathrm{r}}\right|\le\frac{h_{\mathrm{m}}}{2},0\le\gamma_{q,b,j}\le 1\right)\right)}_{T_3}d\mathrm{R}_{x''}d\mathrm{R}_{z''}
\end{aligned}\tag{51}$$

Consequently, the irradiance expression can be expressed based on (52) as

$$E^t_{\mathrm{D,PS}} = \lim_{\substack{w_\mathrm{s}\to 0,\\ \ell_\mathrm{s}\to 0}} \sum_{k=1}^{n_t}\sum_{\ell=1}^{n_t} \iint_{\mathcal{R}^t_{k,\ell}} \frac{\rho_t(m+1)p\cos^{m-1}\left(\theta^{\mathrm{I}^t_{\mathrm{R,D}}}_{\mathrm{R}}\right)}{2\pi A_\mathrm{s}\|\mathbf{RD}\|_2^2} \times \cos\left(\theta^{\mathrm{D}}_{\mathrm{R}}\right)\cos\left(\theta^t_{\mathrm{R,D}}\right)\mathbb{I}\left(\mathrm{I}^t_{\mathrm{R,D}}\in\mathcal{S}\right)dA^t_{\mathrm{R}}. \tag{53}$$

By exploiting the infinitesimally small source area, all the quantities depending on R can be considered constant and replaced by their corresponding values at $\mathrm{R}_{k,\ell}$. Hence, the irradiance expression reduces to

$$E^t_{\mathrm{D,PS}} = \sum_{k=1}^{n_t}\sum_{\ell=1}^{n_t} \frac{\rho_t(m+1)p}{2\pi\left\|\mathrm{R}_{k,\ell}\mathrm{D}\right\|_2^2}\cos^m\left(\theta^{\mathrm{S}}_{\mathrm{R}_{k,\ell}}\right)\cos\left(\theta^{\mathrm{D}}_{\mathrm{R}_{k,\ell}}\right) \times \frac{\cos\left(\theta^t_{\mathrm{R}_{k,\ell},\mathrm{D}}\right)}{\cos\left(\theta^{\mathrm{S}}_{\mathrm{R}_{k,\ell}}\right)}\lim_{w_\mathrm{s}\to 0,\ell_\mathrm{s}\to 0}\frac{\bar{A}^t_{k,\ell}}{A_\mathrm{s}}, \tag{54}$$

where $\bar{A}^t_{k,\ell}$ is the area of the portion of $\mathcal{R}^t_{k,\ell}$ that have a non-zero contribution to the irradiance at D. The limit term appearing at the end of the previous expression can be re-written as $\lim_{w_\mathrm{s}\to 0,\ell_\mathrm{s}\to 0}\frac{\bar{A}^t_{k,\ell}}{A_\mathrm{s}} = \frac{dA_\mathrm{R}}{dA_{\mathrm{I}^t_{\mathrm{R,D}}}}|_{\mathrm{R}=\mathrm{R}_{k,\ell}}$, where $dA_{\mathrm{I}^t_{\mathrm{R,D}}}$ represents the differential area around $\mathrm{I}^t_{\mathrm{R,D}}$ from which the incident rays hit $dA_\mathrm{R}$ and get reflected to D as can be seen in Fig. 8(a) and Fig. 8(b). In the following subsections, we derive more particular expressions for the metasurface and mirror array based reflectors.

### 1) MIRROR ARRAY REFLECTOR

We first evaluate $\cdot\frac{dA^{\mathrm{Mi}}_\mathrm{R}}{dA_{\mathrm{I}^{\mathrm{Mi}}_{\mathrm{R,D}}}}|_{\mathrm{R}=\mathrm{R}_{k,\ell}}$ as

$$\left.\frac{dA^{\mathrm{Mi}}_\mathrm{R}}{dA_{\mathrm{I}^{\mathrm{Mi}}_{\mathrm{R,D}}}}\right|_{\mathrm{R}=\mathrm{R}_{k,\ell}} = \left.\frac{d\mathrm{R}_{x''}d\mathrm{R}_{z''}}{d\mathrm{I}^{\mathrm{Mi}}_{\mathrm{R,D},x}d\mathrm{I}^{\mathrm{Mi}}_{\mathrm{R,D},y}}\right|_{\mathrm{R}=\mathrm{R}_{k,\ell}} = \left|J\left(\frac{\mathrm{I}^{\mathrm{Mi}}_{\mathrm{R,D},x},\mathrm{I}^{\mathrm{Mi}}_{\mathrm{R,D},y}}{\mathrm{R}_{x''},\mathrm{R}_{z''}}\right)\right|^{-1}_{\mathrm{R}=\mathrm{R}_{k,\ell}}, \tag{55}$$

where $\mathrm{I}^{\mathrm{Mi}}_{\mathrm{R,D},x} = \boldsymbol{e}_1^{\mathrm{T}}\mathbf{I}^{\mathrm{Mi}}_{\mathrm{R,D}}$ and $\mathrm{I}^{\mathrm{Mi}}_{\mathrm{R,D},y} = \boldsymbol{e}_2^{\mathrm{T}}\mathbf{I}^{\mathrm{Mi}}_{\mathrm{R,D}}$. Using the chain rule of Jacobians, the previous equation can be re-written as

$$\left.\frac{dA^{\mathrm{Mi}}_\mathrm{R}}{dA_{\mathrm{I}^{\mathrm{Mi}}_{\mathrm{R,D}}}}\right|_{\mathrm{R}=\mathrm{R}_{k,\ell}} = \left.\left(\frac{dA^{\mathrm{Mi}}_\mathrm{R}}{d\bar{A}_\mathrm{R}}\frac{d\bar{A}_\mathrm{R}}{dA_{\mathrm{I}^{\mathrm{Mi}}_{\mathrm{R,D}}}}\right)\right|_{\mathrm{R}=\mathrm{R}_{k,\ell}} = \left|J\left(\frac{\mathrm{I}^{\mathrm{Mi}}_{\mathrm{R,D},x},\mathrm{I}^{\mathrm{Mi}}_{\mathrm{R,D},y}}{\mathrm{R}_x,\mathrm{R}_z}\right)\right|_{\mathrm{R}=\mathrm{R}_{k,\ell}} \Bigg/ \left|J\left(\frac{\mathrm{R}_{x''},\mathrm{R}_{z''}}{\mathrm{R}_x,\mathrm{R}_z}\right)\right|^{-1}_{\mathrm{R}=\mathrm{R}_{k,\ell}}, \tag{56}$$

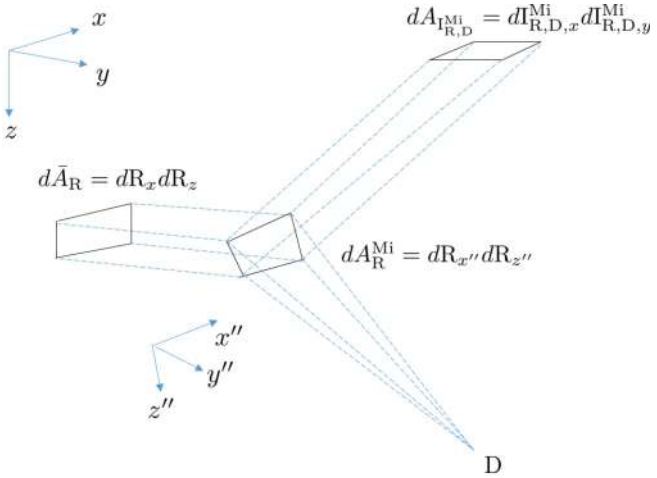


(a) Mirror array reflecting element

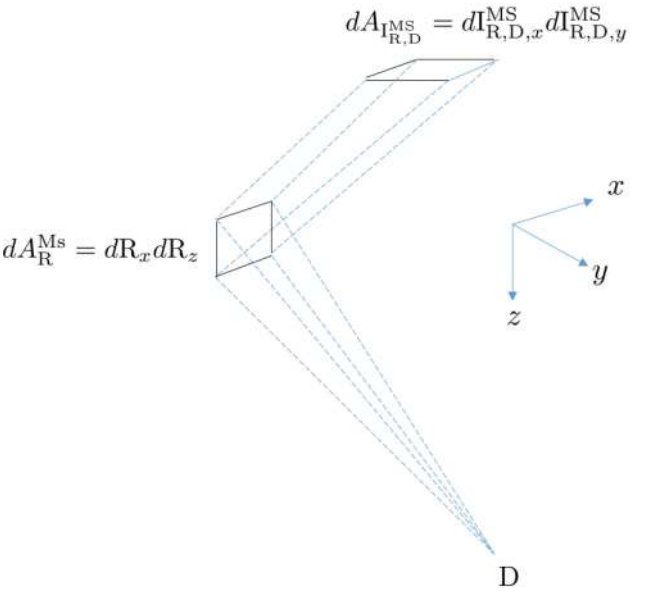


(b) Metasurface reflecting element

**FIGURE 8.** Ratio between differential area elements in reflector and source planes.

where $d\bar{A}_\mathrm{R}$ represents the projection of $dA^{\mathrm{Mi}}_\mathrm{R}$ onto a plane parallel to the $x-z$ plane as depicted in Fig. 8(a). The second Jacobian appearing in the previous expression represents a projection onto the $x-z$ plane. Hence, it can be expressed as

$$J\left(\frac{\mathrm{R}_{x''},\mathrm{R}_{z''}}{\mathrm{R}_x,\mathrm{R}_z}\right) = \frac{1}{\widehat{\mathbf{N}}^{\mathrm{T}}_{k,\ell}\boldsymbol{e}_2}. \tag{57}$$

Using (47), $\mathrm{I}^{\mathrm{Mi}}_{\mathrm{R,D},x}$ and $\mathrm{I}^{\mathrm{Mi}}_{\mathrm{R,D},y}$ are expressed as

$$\mathrm{I}^{\mathrm{Mi}}_{\mathrm{R,D},x} = \mathrm{R}_x + \frac{\mathrm{S}_z-\mathrm{R}_z}{\boldsymbol{e}_3^{\mathrm{T}}\left(\left(2\widehat{\mathbf{N}}^{\mathrm{T}}_{k,\ell}\widehat{\mathrm{RD}}\right)\widehat{\mathbf{N}}_{k,\ell}-\widehat{\mathrm{RD}}\right)} \times \boldsymbol{e}_1^{\mathrm{T}}\left(\left(2\widehat{\mathbf{N}}^{\mathrm{T}}_{k,\ell}\widehat{\mathrm{RD}}\right)\widehat{\mathbf{N}}_{k,\ell}-\widehat{\mathrm{RD}}\right), \tag{58}$$

$$\mathrm{I}^{\mathrm{Mi}}_{\mathrm{R,D},y} = \mathrm{R}_y + \frac{\mathrm{S}_z - \mathrm{R}_z}{\boldsymbol{e}_3^{\mathrm{T}}\Big(\Big(2\widehat{\mathbf{N}}^{\mathrm{T}}_{k,\ell}\widehat{\mathrm{RD}}\Big)\widehat{\mathbf{N}}_{k,\ell} - \widehat{\mathrm{RD}}\Big)} \times \boldsymbol{e}_2^{\mathrm{T}}\Big(\Big(2\widehat{\mathbf{N}}^{\mathrm{T}}_{k,\ell}\widehat{\mathrm{RD}}\Big)\widehat{\mathbf{N}}_{k,\ell} - \widehat{\mathrm{RD}}\Big). \tag{59}$$

Therefore, we can write the Jacobian as

$$\begin{aligned} &J\left(\frac{\mathrm{I}^{\mathrm{Mi}}_{\mathrm{R,D},x}, \mathrm{I}^{\mathrm{Mi}}_{\mathrm{R,D},y}}{\mathrm{R}_x, \mathrm{R}_z}\right)\Bigg|_{\mathrm{R}=\mathrm{R}_{k,\ell}} \\ &= -\frac{\widehat{\mathbf{N}}^{\mathrm{T}}_{k,\ell}\mathbf{RD}\Big(2\widehat{\mathbf{N}}^{\mathrm{T}}_{k,\ell}\boldsymbol{e}_3\widehat{\mathbf{N}}^{\mathrm{T}}_{k,\ell}\mathbf{RD} + \mathrm{S}_z - \mathrm{D}_z\Big)^2}{\widehat{\mathbf{N}}^{\mathrm{T}}_{k,\ell}\boldsymbol{e}_2\Big(2\widehat{\mathbf{N}}^{\mathrm{T}}_{k,\ell}\boldsymbol{e}_3\widehat{\mathbf{N}}^{\mathrm{T}}_{k,\ell}\mathbf{RD} + \mathrm{R}_z - \mathrm{D}_z\Big)^3}\Bigg|_{\mathrm{R}=\mathrm{R}_{k,\ell}} \\ &= -\frac{\widehat{\mathbf{N}}^{\mathrm{T}}_{k,\ell}\mathrm{R}_{k,\ell}\mathbf{D}\big(\|\mathrm{R}_{k,\ell}\mathrm{D}\|_2 + \|\mathrm{R}_{k,\ell}\mathrm{S}\|_2\big)^2\|\mathrm{R}_{k,\ell}\mathrm{S}\|_2}{\widehat{\mathbf{N}}^{\mathrm{T}}_{k,\ell}\boldsymbol{e}_2\|\mathrm{R}_{k,\ell}\mathrm{D}\|_2^3\big(\mathrm{S}_z - \mathrm{R}_{k,\ell,z}\big)}, \end{aligned} \tag{60}$$

where $\mathrm{R}_{k,\ell,z} = \mathrm{R}_{\boldsymbol{k},\boldsymbol{\ell}}{}^{\mathrm{T}}\boldsymbol{e_3}$.

To simplify (54), the ratio $\cos(\theta^{\mathrm{Mi}}_{\mathrm{R}_{k,\ell},\mathrm{D}})/\cos(\theta^{\mathrm{S}}_{\mathrm{R}_{k,\ell}})$ is evaluated as follows

$$\frac{\cos\Big(\theta^{\mathrm{Mi}}_{\mathrm{R}_{k,\ell},\mathrm{D}}\Big)}{\cos\Big(\theta^{\mathrm{S}}_{\mathrm{R}_{k,\ell}}\Big)} = \frac{\widehat{\mathbf{N}}^{\mathrm{T}}_{k,\ell}\mathbf{R}_{k,\ell}\mathbf{D}}{\|\mathbf{R}_{k,\ell}\mathbf{D}\|_2}\frac{\|\mathbf{R}_{k,\ell}\mathbf{S}\|_2}{|\mathrm{S}_z - \mathrm{R}_{k,\ell,z}|}, \tag{61}$$

By substituting (57), (60), and (61) in (54), the mirror array irradiance at D due to point source can be upper bounded by

$$\tilde{E}^{\mathrm{Mi}}_{\mathrm{D,PS}} = \sum_{k=1}^{n_{\mathrm{m}}}\sum_{\ell=1}^{n_{\mathrm{m}}}\frac{\rho_{\mathrm{Mi}}(m+1)p\cos^m\Big(\theta^{\mathrm{S}}_{\mathrm{R}_{k,\ell}}\Big)}{2\pi\big(\|\mathrm{R}_{k,\ell}\mathrm{D}\|_2 + \|\mathrm{R}_{k,\ell}\mathrm{S}\|_2\big)^2}\cos\Big(\theta^{\mathrm{D}}_{\mathrm{R}_{k,\ell}}\Big). \tag{62}$$

Now, we impose small reflector assumptions, where the reflector surface has relatively small solid angles measured at S and D, i.e., $\mathrm{R}_{k,\ell}\ \forall k,\ell$ is almost constant; thus, $\tilde{E}^{\mathrm{Mi}}_{\mathrm{D,PS}}$ can be approximated by $\tilde{E}^{\mathrm{Mi}}_{\mathrm{D,PS}}$ as

$$\tilde{E}^{\mathrm{Mi}}_{\mathrm{D}} = n_{\mathrm{m}}^2\frac{\rho_{\mathrm{Mi}}(m+1)p\cos^m\Big(\theta^{\mathrm{S}}_{\bar{\mathrm{R}}_{\mathrm{Mi}}}\Big)}{2\pi\big(\|\bar{\mathrm{R}}_{\mathrm{Mi}}\mathrm{D}\|_{\mathbf{2}} + \|\bar{\mathrm{R}}_{\mathrm{Mi}}\mathrm{S}\|_{\mathbf{2}}\big)^2}\cos\Big(\theta^{\mathrm{D}}_{\bar{\mathrm{R}}_{\mathrm{Mi}}}\Big), \tag{63}$$

where $\bar{\mathrm{R}}_{\mathrm{Mi}}$ is the centroid of mirror array reflecting elements centers, and $\bar{\mathrm{R}}_{\mathrm{Mi}} = \sum_{k=1}^{n_{\mathrm{m}}}\sum_{\ell=1}^{n_{\mathrm{m}}}\mathrm{R}_{k,\ell}/n_{\mathrm{m}}^2$.

#### 2) METASURFACE REFLECTOR

In a similar approach to the irradiance derivation for the mirror array setup, we first evaluate $\frac{dA^{\mathrm{MS}}_{\mathrm{R}}}{dA^{\mathrm{MS}}_{\mathrm{I_{R,D}}}}|_{\mathrm{R}=\mathrm{R}_{k,\ell}}$ as

$$\frac{dA^{\mathrm{MS}}_{\mathrm{R}}}{dA^{\mathrm{MS}}_{\mathrm{I_{R,D}}}}\Bigg|_{\mathrm{R}=\mathrm{R}_{k,\ell}} = \left|J\left(\frac{\mathrm{I}^{\mathrm{MS}}_{\mathrm{R,D},x}, \mathrm{I}^{\mathrm{MS}}_{\mathrm{R,D},y}}{\mathrm{R}_x, \mathrm{R}_z}\right)\Bigg|_{\mathrm{R}=\mathrm{R}_{k,\ell}}\right|^{-1}, \tag{64}$$

where

$$\mathrm{I}^{\mathrm{MS}}_{\mathrm{R,D},y} = -\mathrm{D}_y + \frac{(h_{\mathrm{d}}-\Delta_z)\sqrt{\ell^2_{\mathrm{RD}} - \Big(\Delta_x - c^x_{k,\ell}\ell_{\mathrm{RD}}\Big)^2 - \Big(\Delta_z - c^z_{k,\ell}\ell_{\mathrm{RD}}\Big)^2}}{\Delta_z - c^z_{k,\ell}\ell_{\mathrm{RD}}},$$

$$\mathrm{I}^{\mathrm{MS}}_{\mathrm{R,D},x} = \Delta_x + \frac{(h_{\mathrm{d}}-\Delta_z)\Big(\Delta_x - c^x_{k,\ell}\ell_{\mathrm{RD}}\Big)}{\Delta_z - c^z_{k,\ell}\ell_{\mathrm{RD}}},$$

such that $\Delta_x = \mathrm{R}_x - \mathrm{D}_x$, $\Delta_z = \mathrm{R}_z - \mathrm{D}_z$, and $\ell_{\mathrm{RD}} = \sqrt{(\mathrm{R}_x - \mathrm{D}_x)^2 + \mathrm{D}_y^2 + (\mathrm{R}_z - \mathrm{D}_z)^2}$. Finally, the irradiance of the metasurface reflector at D due to point source is found to be

$$E^{\mathrm{MS}}_{\mathrm{D,PS}} = \sum_{k=1}^{n_{\mathrm{p}}}\sum_{\ell=1}^{n_{\mathrm{p}}}\frac{\rho_{\mathrm{MS}}(m+1)p\cos^{m-1}\Big(\theta^{\mathrm{S}}_{\mathrm{R}_{k,\ell}}\Big)}{2\pi\|\mathrm{R}_{k,\ell}\mathrm{D}\|_2^2}\cos\Big(\theta^{\mathrm{MS}}_{\mathrm{R}_{k,\ell},\mathrm{D}}\Big) \times \cos\Big(\theta^{\mathrm{D}}_{\mathrm{R}_{k,\ell}}\Big)\Big/\left|J\left(\frac{\mathrm{I}^{\mathrm{MS}}_{\mathrm{R,D},x}, \mathrm{I}^{\mathrm{MS}}_{\mathrm{R,D},y}}{\mathrm{R}_x, \mathrm{R}_z}\right)|_{\mathrm{R}=\mathrm{R}_{k,\ell}}\right|. \tag{65}$$

By approximating the Jacobian term in (65) with its mirror array counter part, $E^{\mathrm{MS}}_{\mathrm{D,PS}}$ can be approximated by $\bar{E}^{\mathrm{MS}}_{\mathrm{D,PS}}$ given by

$$\bar{E}^{\mathrm{MS}}_{\mathrm{D,PS}} = \sum_{k=1}^{n_{\mathrm{p}}}\sum_{\ell=1}^{n_{\mathrm{p}}}\frac{\rho_{\mathrm{MS}}(m+1)p\cos^m\Big(\theta^{\mathrm{S}}_{\mathrm{R}_{k,\ell}}\Big)}{2\pi\big(\|\mathrm{R}_{k,\ell}\mathrm{D}\|_2 + \|\mathrm{R}_{k,\ell}\mathrm{S}\|_2\big)^2} \times \frac{\cos\Big(\theta^{\mathrm{D}}_{\mathrm{R}_{k,\ell}}\Big)\cos\Big(\theta^{\mathrm{MS}}_{\mathrm{R}_{k,\ell},\mathrm{D}}\Big)}{\widehat{\mathbf{N}}^{\mathrm{T}}_{k,\ell}\widehat{\mathbf{R}_{k,\ell}\mathbf{D}}}. \tag{66}$$

Using the small reflector assumption brings a further simplification by approximating $\bar{E}^{\mathrm{MS}}_{\mathrm{D,PS}}$ with $\tilde{E}^{\mathrm{MS}}_{\mathrm{D,PS}}$ expressed as

$$\tilde{E}^{\mathrm{MS}}_{\mathrm{D,PS}} = \frac{\rho_{\mathrm{MS}}(m+1)p\cos^m\Big(\theta^{\mathrm{S}}_{\bar{\mathrm{R}}_{\mathrm{MS}}}\Big)}{2\pi\big(\|\bar{\mathrm{R}}_{\mathrm{MS}}\mathrm{D}\|_{\mathbf{2}} + \|\bar{\mathrm{R}}_{\mathrm{MS}}\mathrm{S}\|_{\mathbf{2}}\big)^2} \times \frac{\cos\Big(\theta^{\mathrm{D}}_{\bar{\mathrm{R}}_{\mathrm{MS}}}\Big)\cos\Big(\theta^{\mathrm{MS}}_{\bar{\mathrm{R}}_{\mathrm{MS}},\mathrm{D}}\Big)}{\bar{\mathbf{N}}^{\mathrm{T}}\widehat{\bar{\mathrm{R}}_{\mathrm{MS}}\mathbf{D}}}n_{\mathrm{p}}{}^2, \tag{67}$$

where $\bar{\mathrm{R}}_{\mathrm{MS}}$ represents the centroid of the metasurface reflector, $\bar{\mathrm{R}}_{\mathrm{MS}} = \sum_{k=1}^{n_{\mathrm{p}}}\sum_{\ell=1}^{n_{\mathrm{p}}}\mathrm{R}_{k,\ell}/n_{\mathrm{p}}^2$, and $\bar{\mathbf{N}} = (\frac{\bar{\mathrm{R}}_{\mathrm{MS}}\mathrm{S}}{\|\bar{\mathrm{R}}_{\mathrm{MS}}\mathrm{S}\|_2} + \frac{\bar{\mathrm{R}}_{\mathrm{MS}}\mathrm{D}}{\|\bar{\mathrm{R}}_{\mathrm{MS}}\mathrm{D}\|_2})/\sqrt{2 + 2\frac{\bar{\mathrm{R}}_{\mathrm{MS}}\mathrm{D}^{\mathrm{T}}\bar{\mathrm{R}}_{\mathrm{MS}}\mathrm{S}}{\|\bar{\mathrm{R}}_{\mathrm{MS}}\mathrm{D}\|_2\|\bar{\mathrm{R}}_{\mathrm{MS}}\mathrm{S}\|_2}}}$.

### *B. LARGE SOURCE SMALL REFLECTOR CASE*

In this case, we assume the reflector largest dimension to be much smaller than the minimum distance between a point on the reflector and a point on the source, and the minimum distance between a point on the reflector and D. Also, we presume a large enough source such that all the incident rays on the reflector reaching D originate within $\mathcal{S}$. Based on the previous assumptions, $\theta^{I_{\mathrm{R,D}}}_{\mathrm{R}}$, $\theta^{\mathrm{D}}_{\mathrm{R}}$, and $\theta^{t}_{\mathrm{R,D}}$ $\forall \mathrm{R} \in \mathcal{R}^t_{k,\ell}$ can be approximated by $\theta^{\mathrm{S}}_{\mathrm{R}_{k,\ell}}$, $\theta^{\mathrm{P}}_{\mathrm{R}_{k,\ell}}$, and $\theta^{t}_{\mathrm{R}_{k,\ell},\mathrm{D}}$, respectively, and RD $\forall \mathrm{R} \in \mathcal{R}^t_{k,\ell}$ can be approximated by $\mathrm{R}_{k,\ell}\mathrm{D}$. Furthermore,

$\iint_{\mathcal{R}^t_{k,\ell}} \mathbb{I}(\mathrm{I}_{\mathrm{R,D}} \in \mathcal{S}) dA_{\mathrm{R}} = w_t h_t$. Consequently, $E^t_{\mathrm{D}}$ in (52) reduces to

$$E^t_{\mathrm{D,LSSR}} = \rho_t w_t h_t \sum_{k=1}^{n_t} \sum_{\ell=1}^{n_t} \frac{(m+1)p\cos^{m-1}\left(\theta^{\mathrm{S}}_{\mathrm{R}_{k,\ell}}\right)}{2\pi A_{\mathrm{s}} \|\mathbf{R}_{k,\ell}\mathbf{D}\|_2^2} \times \cos\left(\theta^{\mathrm{P}}_{\mathrm{R}_{k,\ell}}\right) \cos\left(\theta^t_{\mathrm{R}_{k,\ell},\mathrm{D}}\right). \quad (68)$$

If the setup geometry strongly satisfies the small reflector assumption, $E^t_{\mathrm{D,LSSR}}$ can be further approximated by $\bar{E}^t_{\mathrm{D,LSSR}}$, expressed as

$$\bar{E}^t_{\mathrm{D,LSSR}} = \rho_t w_t h_t n_t^2 \frac{(m+1)p\cos^{m-1}\left(\theta^{\mathrm{S}}_{\bar{\mathrm{R}}_t}\right)}{2\pi A_{\mathrm{s}} \|\bar{\mathrm{R}}_t\mathbf{D}\|_2^2} \times \cos\left(\theta^{\mathrm{P}}_{\bar{\mathrm{R}}_t}\right) \cos\left(\theta^t_{\bar{\mathrm{R}}_t,\mathrm{D}}\right). \quad (69)$$

## VII. ANALYTICAL INSIGHTS

In this section, we consider the small reflector regime and manifest the power focusing capability for both reflectors. Moreover, we provide design guidelines regarding the proper selection of reflector type based on the setup geometry.

### A. POWER CONCENTRATION CAPABILITY ANALYSIS

The small reflector regime allows us to express $E_{\mathrm{D}}$ in (52) at the detector center as

$$\bar{E}^t_{\mathrm{D,SR}} = \rho_t n_t^2 \frac{(m+1)p\cos^{m-1}\left(\theta^{\mathrm{S}}_{\bar{\mathrm{R}}_t}\right)}{2\pi A_{\mathrm{s}} \|\bar{\mathrm{R}}_t\mathbf{D}\|_2^2} \times \cos\left(\theta^{\mathrm{P}}_{\bar{\mathrm{R}}_t}\right) \cos\left(\theta^t_{\bar{\mathrm{R}}_t,\mathrm{D}}\right) A_{\bar{\mathrm{R}}_t}, \quad (70)$$

where $\bar{\mathcal{R}}^t$ represents the set of points of a virtual reflecting element centered at $\bar{\mathrm{R}}$, where $|\bar{\mathcal{R}}^t| = w_t h_t$, and $A_{\bar{\mathrm{R}}_t} = \iint_{\bar{\mathcal{R}}^t} \mathbb{I}(\mathrm{I}_{\mathrm{R,D}} \in \mathcal{S}) dA_{\mathrm{R}}$ represents the effective reflection area contributing to the irradiance at D. By assuming tightly packed reflectors ($\Delta w_{\mathrm{p}} = \Delta w_{\mathrm{m}} = \Delta h_{\mathrm{p}} = \Delta h_{\mathrm{m}} = 0$), the total width and height become, respectively, $W_{\mathrm{T}} = n_t w_t$ and $H_{\mathrm{T}} = n_t h_t$. By defining the set $\mathcal{S}_{\bar{\mathrm{R}}_t,\mathrm{D}}$ as $\{\mathrm{R} : \mathrm{R} \in$ the plane containing $\bar{\mathcal{R}}^t, \mathrm{I}^t_{\mathrm{R,D}} \in \mathcal{S}\}$, it is evident that $A_{\bar{\mathrm{R}}_t} = |\mathcal{S}_{\bar{\mathrm{R}},\mathrm{D}} \cap \bar{\mathcal{R}}^t|$. It is clear that for a fixed detector location, $n_t$, $A_{\mathrm{s}}$, and $A_{\bar{\mathrm{R}}_t}$ are the main controllers of $\bar{E}_{\mathrm{D,SR}}$. By considering a relatively small source, where $|\mathcal{S}_{\bar{\mathrm{R}},\mathrm{D}}| << |\bigcup_{k,\ell} \mathcal{R}^t_{k,\ell}|$, $|\mathcal{S}_{\bar{\mathrm{R}},\mathrm{D}}| \approx A_{\mathrm{s}} / \frac{dA_{\mathrm{I}^t_{\mathrm{R,D}}}}{dA^t_{\mathrm{R}}}|_{\mathrm{R}=\bar{\mathrm{R}}_{\mathrm{t}}}$. The following can be deduced:

- For small enough $n_t$, $\mathcal{S}_{\bar{\mathrm{R}},\mathrm{D}} \subseteq \bar{\mathcal{R}}^t$, $A_{\bar{\mathrm{R}}_t} = |\mathcal{S}_{\bar{\mathrm{R}},\mathrm{D}}| \approx A_{\mathrm{s}} / \frac{dA_{\mathrm{I}^t_{\mathrm{R,D}}}}{dA^t_{\mathrm{R}}}|_{\mathrm{R}=\bar{\mathrm{R}}_{\mathrm{t}}}$ (independent on $n_t$), and hence $\bar{E}_{\mathrm{D,SR}}$ increases linearly with $n_t^2$. (Similar results are deduced for very small $A_{\mathrm{s}}$)
- For asymptotically large $n_t$, $\bar{\mathcal{R}}^t \subseteq \mathcal{S}_{\bar{\mathrm{R}},\mathrm{D}}$, hence, $A_{\bar{\mathrm{R}}_t} = |\bar{\mathcal{R}}^t| = W_{\mathrm{T}} H_{\mathrm{T}} / n_t^2$ and $\bar{E}_{\mathrm{D,SR}}$ becomes independent on $n_t$. (Similar results are deduced for very large $A_{\mathrm{s}}$)

The irradiance increase at D confirms the power focusing capability of the proposed reflectors. This owes to the constancy of the total reflected power, as the reflectors areas are kept constant when $n_t$ increases. Based on the previous discussion, the smaller the source area with respect to the total reflector area, the better power focusing performance, i.e., if the source area is large enough, regardless of the number of reflecting elements, the received power will be almost the same. It is worth mentioning that only in the point source regime, the power can be focused without limits; in this case, the irradiance at D becomes infinite, and zero everywhere else such that the received power equals the total reflected power.

### B. POWER ANALYSIS

The source radiates a total of $p$ watts, $p_{\mathrm{inc}}$ of which is incident on the reflector. Then only $\rho_t p_{\mathrm{inc}}$ is reflected towards the detection plane. Finally, the total received power by the detector denoted by $p^{\mathrm{t}}_{\mathrm{rx}}$ can be expressed using (3) as

$$p^{\mathrm{t}}_{\mathrm{rx}} = \int_{x_{\mathrm{d}}-\frac{w_{\mathrm{d}}}{2}}^{x_{\mathrm{d}}+\frac{w_{\mathrm{d}}}{2}} \int_{y_{\mathrm{d}}-\frac{\ell_{\mathrm{d}}}{2}}^{y_{\mathrm{d}}+\frac{\ell_{\mathrm{d}}}{2}} E^{\mathrm{t}}_{\mathrm{P}}(x_{\mathrm{p}}, y_{\mathrm{p}}) dx_{\mathrm{p}} dy_{\mathrm{p}}. \quad (71)$$

If the detector area is small with respect to the source image in the detector plane $\mathcal{S}' = \{\mathrm{P} : \boldsymbol{e}_3^{\mathrm{T}}\mathbf{P} = h_{\mathrm{d}}, \exists \mathrm{R} \in \bigcup_{k,\ell} \mathcal{R}^t_{k,\ell}$ where $\mathrm{I}_{\mathrm{R,P}} \in \mathcal{S}\}$, $p^{\mathrm{t}}_{\mathrm{rx}}$ can be approximated by

$$\tilde{p}^{\mathrm{t}}_{\mathrm{rx}} = E^{\mathrm{t}}_{\mathrm{P}}(x_{\mathrm{d}}, y_{\mathrm{d}}) w_{\mathrm{d}} \ell_{\mathrm{d}}. \quad (72)$$

For a small source, small reflector scenario $p_{\mathrm{inc}}$ can be approximated as

$$\tilde{p}_{\mathrm{inc}} = \frac{(m+1)p\cos^{m}\left(\theta^{\mathrm{S}}_{\bar{\mathrm{R}}_t}\right) n_t^2 w_t h_t \cos\left(\theta^{\mathrm{i}}_{\bar{\mathrm{R}}_t,\mathrm{I}^t_{\bar{\mathrm{R}}_t,\mathrm{D}}}\right)}{2\pi \|\mathbf{S}\bar{\mathrm{R}}_t\|_2^2}. \quad (73)$$

The received power from the direct LoS path assuming point source, can be approximated by

$$p_{\mathrm{LoS}} = \frac{(m+1)p\cos^{m+1}(\theta_{\mathrm{D}})}{2\pi \|\mathbf{SD}\|_2^2} w_{\mathrm{d}} \ell_{\mathrm{d}}, \quad (74)$$

where $\theta_{\mathrm{D}}$ represents the angle between $\boldsymbol{e}_2$ and SD. In the very ideal asymptotic case, where a point source is considered and $n_t \to \infty$, the total reflected power is focused at D and the total received power from reflection $p^{\mathrm{t}}_{\mathrm{rx,\,PS}} = \rho_t p_{\mathrm{inc}}$.

### C. REFLECTORS RELATIVE PERFORMANCE ANALYSIS

The fundamental difference between metasurfaces and ordinary mirrors is the relationship between the reflected rays and their corresponding incident rays directions. For ordinary mirrors, the volume occupied in the space of directions by a bundle of rays incident at the same point, is the same as that occupied by their corresponding reflected rays. Nonetheless, the non-linear relationship between the polar and the azimuth angles of reflection $\theta'$, $\phi'$ and their corresponding incidence angles $\theta^{\mathrm{i}}$, $\phi^{\mathrm{i}}$, respectively, enforced by the generalized law of reflection governing metasurfaces response, alters this fact. To account for this effect, we define the beam spread ratio (B$SR$) metric as

$$\mathrm{BSR} \triangleq \frac{d\omega'}{d\omega_i}, \quad (75)$$

where $d\omega'$ is the differential solid angle occupied by the reflected ray bundle at the reflection direction defined by $\theta'$, $\phi'$ and their corresponding incident ray bundle occupying $d\omega_{\rm i}$ at the direction defined by $\theta^{\rm i}$,$\phi^{\rm i}$. So, we write the metasurface reflector as (for proof see Appendix C)

$$\mathrm{BSR_{MS}} = \frac{\cos\left(\theta^{\rm i}\right)}{\cos(\theta')}. \tag{76}$$

One can show easily that $\frac{d\omega'}{d\omega_i} = 1$ for all reflector points of the mirror array. Intuitively, the irradiance and thus the received power at the detector (for a small detector) are proportional to the reflected beam intensity (RBI), defined as the amount of reflected power per-solid angle measured along the line connecting the reflector and the detector centers, which is expressed as

$$\begin{aligned}\mathrm{RBI}_t &= \frac{p^t_{\rm ref}}{\omega'_t} = \rho_t p^t_{\rm inc} \frac{\frac{A_{\bar{\mathrm{R}}_t}}{w_t h_t}}{\omega'_t} \\ &\approx \frac{\rho_t (m+1) p \cos^m\left(\theta^{\rm S}_{\bar{\mathrm{R}}_t}\right) n_t^2 \cos\left(\theta^{\rm i}_{\mathrm{I}^t_{\bar{\mathrm{R}}_t,\mathrm{D}}}\right)}{2\pi \left\|\mathbf{S}\bar{\mathbf{R}}_t\right\|_2^2} \frac{A_{\bar{\mathrm{R}}_t}}{\omega'_t},\end{aligned} \tag{77}$$

where $\omega'_t$ represents the solid angle subtended by the detector measured at $\bar{\mathrm{R}}_t$. To assess the relative systems performance, we consider two reflectors having the same area, number of reflecting elements, and reflection efficiency and compute the RBI ratio (RBIR) of the two systems as

$$\begin{aligned}\mathrm{RBIR} &= \frac{p^{\rm MS}_{\rm ref}}{\omega'_{\rm MS}} \Big/ \frac{p^{\rm Mi}_{\rm ref}}{\omega'_{\rm Mi}} \approx \frac{\cos\left(\theta^{\rm i}_{\bar{\mathrm{R}}_{\rm MS},\mathrm{I}^{\rm MS}_{\bar{\mathrm{R}}_{\rm MS},\mathrm{D}}}\right)}{\cos\left(\theta^{\rm i}_{\bar{\mathrm{R}}_{\rm Mi},\mathrm{I}^{\rm Mi}_{\bar{\mathrm{R}}_{\rm Mi},\mathrm{D}}}\right)} \frac{A_{\bar{\mathrm{R}}_{\rm MS}}}{A_{\bar{\mathrm{R}}_{\rm Mi}}} \frac{\omega'_{\rm Mi}}{\omega^{\rm i}_{\rm MS}} \frac{\omega^{\rm i}_{\rm MS}}{\omega'_{\rm MS}} \\ &= \frac{\cos\left(\theta^{\rm i}_{\bar{\mathrm{R}}_{\rm MS},\mathrm{I}^{\rm MS}_{\bar{\mathrm{R}}_{\rm MS},\mathrm{D}}}\right)}{\cos\left(\theta^{\rm i}_{\bar{\mathrm{R}}_{\rm Mi},\mathrm{I}^{\rm Mi}_{\bar{\mathrm{R}}_{\rm Mi},\mathrm{D}}}\right)} \frac{A_{\bar{\mathrm{R}}_{\rm MS}}}{A_{\bar{\mathrm{R}}_{\rm Mi}}} \frac{1}{\mathrm{BSR_{MS}}}.\end{aligned} \tag{78}$$

For large $n_{\rm p}, n_{\rm m}$ the RBIR reduces to

$$\mathrm{RBIR} = \frac{\cos\left(\theta^{\rm i}_{\bar{\mathrm{R}}_{\rm MS},\mathrm{I}^{\rm MS}_{\bar{\mathrm{R}}_{\rm MS},\mathrm{D}}}\right)}{\cos\left(\theta^{\rm i}_{\bar{\mathrm{R}}_{\rm Mi},\mathrm{I}^{\rm Mi}_{\bar{\mathrm{R}}_{\rm Mi},\mathrm{D}}}\right)} \frac{1}{\mathrm{BSR_{MS}}} = \frac{\cos\left(\theta^{\rm MS}_{\bar{\mathrm{R}}_{\rm MS},\mathrm{D}}\right)}{\cos\left(\theta^{\rm i}_{\bar{\mathrm{R}}_{\rm Mi},\mathrm{I}^{\rm Mi}_{\bar{\mathrm{R}}_{\rm Mi},\mathrm{D}}}\right)}. \tag{79}$$

As for the performance merit of employing the proposed reflectors, we define $G_{\rm MS} \triangleq \tilde{p}^{\rm MS}_{\rm rx}/p_{\rm LoS}$ and $G_{\rm Mi} \triangleq \tilde{p}^{\rm Mi}_{\rm rx}/p_{\rm LoS}$ to represent the received power gain of metasurface and mirror array, respectively, compared with an IRS-free system depending on the received LoS power. For the small reflector regime, the gain can be expressed as

$$G_t = \frac{\rho_t n_t^2 \cos^{m-1}\left(\theta^{\rm S}_{\bar{\mathrm{R}}_t}\right) \cos\left(\theta^{\rm P}_{\bar{\mathrm{R}}_t}\right) \cos\left(\theta^t_{\bar{\mathrm{R}}_t,\mathrm{D}}\right) \|\mathbf{SD}\|_2^2 A_{\bar{\mathrm{R}}_t}}{A_{\rm s} \cos^{m+1}(\theta_{\rm D}) \left\|\bar{\mathbf{R}}_t\mathbf{D}\right\|_2^2}. \tag{80}$$

For large $n_{\rm t}$, $G_t$ can be approximated by $\tilde{G}_t$ as

$$\begin{aligned}\tilde{G}_t &= \rho_t n_t^2 \frac{\cos^{m-1}\left(\theta^{\rm S}_{\bar{\mathrm{R}}_t}\right) \cos\left(\theta^{\rm P}_{\bar{\mathrm{R}}_t}\right) \cos\left(\theta^t_{\bar{\mathrm{R}}_t,\mathrm{D}}\right) \|\mathbf{SD}\|_2^2}{A_{\rm s} \cos^{m+1}(\theta_{\rm D}) \|\bar{\mathbf{R}}_t\mathbf{D}\|_2^2} w_t h_t \\ &= \rho_t n_t^2 \frac{\cos^{m-1}\left(\theta^{\rm S}_{\bar{\mathrm{R}}_t}\right) \left(h_{\rm d} - \bar{\mathrm{R}}_z\right) \cos\left(\theta^t_{\bar{\mathrm{R}}_t,\mathrm{D}}\right) \|\mathbf{SD}\|_2^{m+3}}{A_{\rm s} \left\|\bar{\mathbf{R}}_t\mathbf{D}\right\|_2^3 h_{\rm d}^{m+1}} w_t h_t.\end{aligned} \tag{81}$$

It can be noticed that, $\frac{\theta^{\rm i}_{\bar{\mathrm{R}}_{\rm MS},\mathrm{I}^{\rm MS}_{\bar{\mathrm{R}}_{\rm MS},\mathrm{D}}}}{2} \le \theta^{\rm Mi}_{\bar{\mathrm{R}}_{\rm Mi},\mathrm{D}} \le \frac{\pi}{4} + \frac{\theta^{\rm i}_{\bar{\mathrm{R}}_{\rm MS},\mathrm{I}^{\rm MS}_{\bar{\mathrm{R}}_{\rm MS},\mathrm{D}}}}{2}$. Moreover, $h_{\rm d} \le \|\mathbf{SD}\|_2 \le \|\bar{\mathbf{R}}_t\mathbf{D}\|_2 + \|\bar{\mathbf{R}}_t\mathbf{S}\|_2$. Hence, the achievable gain using the proposed reflectors can be bounded as

$$\begin{aligned}&\frac{\rho_t n_t^2 w_t h_t \cos^{m-1}\left(\theta^{\rm S}_{\bar{\mathrm{R}}_t}\right) \left(h_{\rm d} - \bar{\mathrm{R}}_z\right) \cos\left(\theta^t_{\bar{\mathrm{R}}_t,\mathrm{D}}\right) h_{\rm d}^2}{A_{\rm s} \left\|\bar{\mathbf{R}}_t\mathbf{D}\right\|_2^3} \le \tilde{G}_t \\ &\le \frac{\rho_t n_t^2 w_t h_t \cos^{m-1}\left(\theta^{\rm S}_{\bar{\mathrm{R}}_t}\right) \left(h_{\rm d} - \bar{\mathrm{R}}_z\right) \cos\left(\theta^t_{\bar{\mathrm{R}}_t,\mathrm{D}}\right) \left(\|\bar{\mathbf{R}}_t\mathbf{D}\|_2 + \|\bar{\mathbf{R}}_t\mathbf{S}\|_2\right)^{m+3}}{A_{\rm s} \|\bar{\mathbf{R}}_t\mathbf{D}\|_2^3 h_{\rm d}^{m+1}}.\end{aligned}$$

The upper bound in the previous inequality becomes exact as $r^t_{\rm d}$ increases asymptotically. In such regime, that upper bound reduces to

$$\begin{aligned}\tilde{G}_t \approx \Bigg(&\rho_t n_t^2 w_t h_t \cos^{m-1}\left(\theta^{\rm S}_{\bar{\mathrm{R}}_t}\right) \left(h_{\rm d} - \bar{\mathrm{R}}_z\right) \cos\left(\theta^t_{\bar{\mathrm{R}}_t,\mathrm{D}}\right) \\ &\times \left(\left(r^t_{\rm d}\right)^2 + \left(h_{\rm d} - \bar{\mathrm{R}}_z\right)\right)^{\frac{m}{2}}\Bigg) \Big/ \left(A_{\rm s} h_{\rm d}^{m+1}\right).\end{aligned} \tag{82}$$

Based on the previous equation, it can be deduced that $\tilde{G}_{\rm Mi}$ grows unboundedly with $r^{\rm Mi}_{\rm d}$. This attributes to the independence of the $\theta^{\rm Mi}_{\bar{\mathrm{R}}_{\rm Mi},\mathrm{D}}$ bounds on $r^{\rm Mi}_{\rm d}$. As for the metasurface reflector, $\tilde{G}_{\rm MS}$ can be expressed for large $r^{\rm MS}_{\rm d}$ as

$$\begin{aligned}\tilde{G}_{\rm MS} \approx \Bigg(&\rho_{\rm MS} n_{\rm p}^2 w_{\rm p} h_{\rm p} \cos^{m-1}\left(\theta^{\rm S}_{\bar{\mathrm{R}}_{\rm MS}}\right) \left(h_{\rm d} - \bar{\mathrm{R}}_z\right) r^{\rm MS}_{\rm d} \sin\left(\phi^{\rm MS}_{\rm d}\right) \\ &\times \left(\left(r^{\rm MS}_{\rm d}\right)^2 + \left(h_{\rm d} - \bar{\mathrm{R}}_z\right)\right)^{\frac{m-1}{2}}\Bigg) \Big/ \left(A_{\rm s} h_{\rm d}^{m+1}\right).\end{aligned} \tag{83}$$

Consequently, $\tilde{G}_{\rm MS}$ grows unboundedly as $r^{\rm MS}_{\rm d}$ increases asymptotically.

Before moving to the simulations discussion, it is worth highlighting some possible challenges that might arise as a result of incorporating IRSs in VLC setups and presenting some possible solutions. For instance, the focused power reaching the photodetector might lead to saturation, and the communication link failure consequently. Two ways can address this issue; pre-deployment and post-deployment solutions. The former involves selecting the IRS location and dimensions properly; thus, the maximum level received power at the points of interest does not exceed the photodetector saturation level. In the post-deployment solution, the reflecting elements are divided into two complementary sets, namely, the active set and the inactive set. The former represents the reflecting elements participating in focusing the incident power towards the photodetector. On the other

**TABLE 2.** Default simulation parameters.

| | | | |
|---|---|---|---|
| $p = 20$ W | $l_{\mathrm{s}} = 1$ cm | $w_{\mathrm{s}} = 1$ cm | $m = 2$ |
| $x_{\mathrm{d}} = 0$ m | $y_{\mathrm{d}} = 2$ m | $h_{\mathrm{d}} = 3$ m | $l_{\mathrm{d}} = 1$ cm |
| $n_{\mathrm{p}} = 10$ | $w_{\mathrm{p}} = 2.5$ cm | $h_{\mathrm{p}} = 1.5$ cm | $n_{\mathrm{m}} = 10$ |
| $\Delta_{h_{\mathrm{p}}} = 0$ cm | $\Delta_{w_{\mathrm{p}}} = 0$ cm | $\Delta_{h_{\mathrm{m}}} = 0$ cm | $\Delta_{w_{\mathrm{m}}} = 0$ cm |
| $x_{\mathrm{s}} = -0.125$ m | $y_{\mathrm{s}} = 2$ m | $w_{\mathrm{d}} = 1$ cm | $z_{\mathrm{s}} = 1.0212$ m |
| $w_{\mathrm{m}} = 2.5$ cm | $h_{\mathrm{m}} = 1.5$ cm | $\rho_t = 0.8$ | $\phi_{\mathrm{d}}^t = \pi/2$ |

hand, the inactive set represents the rest of the reflecting elements that are tuned to direct the incident power away from the photodetector. By proper selection of elements of the two sets, photodetector saturation can be avoided easily. Moreover, the unintentionally received power in an indoor IRS-aided VLC scenario at the detector from the ceiling (outside the source boundaries) diffused reflections through the IRS might result in inter-symbol interference. Nonetheless, this portion of power is negligible for small IRSs where the area of the set of ceiling points contributing to the unintentionally received power is small. Also, these points distribute the reflected power evenly over all the directions. Hence, the photodetector share of this reflected power is minimal.

## VIII. SIMULATION RESULTS

In this section, we evaluate the performance of the two proposed reflectors through several simulations. Specifically, we study the impact of the detector location and the number of reflecting elements (metasurface patches/mirrors) on the total received optical power. We use the global coordinate system assumed in Section IV-B (where $\bar{\mathrm{S}}$ represents the origin as shown in Fig. 6), and assume the system parameter values provided in Table 2; unless otherwise stated. We assume a small detector regime for most of the presented received optical power results. Hence, (72) is the default equation used in evaluating the received power.

In the first simulation, we study the impact of detector location on the received optical power by comparing the reflectors' gain performance with the LoS link. To this end, we focus on small reflectors with a large number of elements ($n_{\mathrm{m}} = n_{\mathrm{p}} = 25$) scenario and plot $\tilde{G}_{\mathrm{MS}}$, $\tilde{G}_{\mathrm{Mi}}$, respectively, computed using (81) in Fig. 9(a), Fig. 9(b). In this simulation, we set $y_{\mathrm{s}} = 0.5$ to highlight the setup geometry effect on the RBIR. Moreover, we set $w_{\mathrm{p}} = w_{\mathrm{m}} = 1$cm and $h_{\mathrm{p}} = h_{\mathrm{m}} = 0.6$ cm to keep the total compact reflector width and height 25 cm and 15 cm, respectively. In addition, $\Delta_{w_{\mathrm{m}}} = 2w_{\mathrm{m}}$, and $\Delta_{h_{\mathrm{m}}} = 2h_{\mathrm{m}}$ to reduce the inter-element blockage effect. One can see from Fig. 9(a) that $\tilde{G}_{\mathrm{MS}}$ is very small for the detector locations that are very close to the reflector plane, i.e., $r_{\mathrm{d}}^{\mathrm{MS}} \approx 0$. This attributes to the large $\theta^{\mathrm{MS}}_{\bar{\mathrm{R}}_{\mathrm{MS}},\mathrm{D}}$, leading to large B$SR_{\mathrm{MS}}$ and consequently small irradiance at the detector, which can be also seen in the $\cos(\theta^{\mathrm{MS}}_{\bar{\mathrm{R}}_{\mathrm{MS}},\mathrm{D}})$ term appearing in (81). Moreover, the proved unbounded received power gains for large $r_{\mathrm{d}}^{\mathrm{MS}}$ and $r_{\mathrm{d}}^{\mathrm{Mi}}$ are numerically verified for both reflectors in Fig. 9(a) and Fig. 9(b). Interestingly, in contrast to the metasurface reflector, $\tilde{G}_{\mathrm{Mi}}$ does not vanish as $r_{\mathrm{d}}^{\mathrm{Mi}}$ becomes very small. This owes to the principle of operation of the mirror array

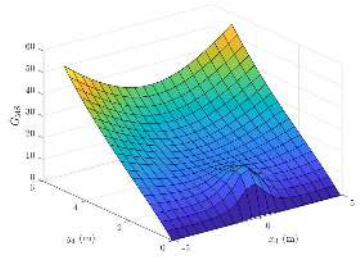

(a) Metasurface to LoS received power ratio at the detector

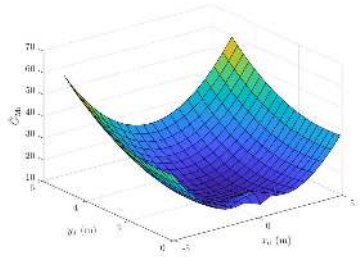

(b) Mirror array to LoS received power ratio at the detector

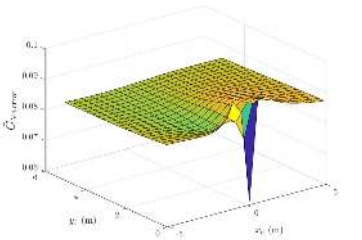

(c) Relative error between $\tilde{G}_{\mathrm{Mi}}$ and $\frac{p_{\mathrm{rx,U}}^{\mathrm{Mi}}}{p_{\mathrm{LoS}}}$

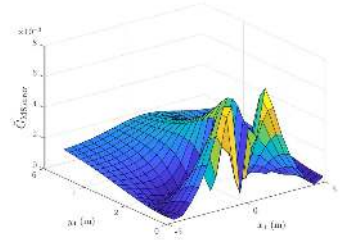

(d) Relative error between $\tilde{G}_{\mathrm{MS}}$ and $\frac{p_{\mathrm{rx}}^{\mathrm{MS}}}{p_{\mathrm{LoS}}}$

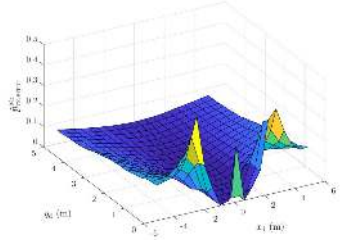

(e) Relative error between $p_{\mathrm{rx}}^{\mathrm{Mi}}$ and $p_{\mathrm{rx,U}}^{\mathrm{Mi}}$

**FIGURE 9.** Received power distribution vs detector location.

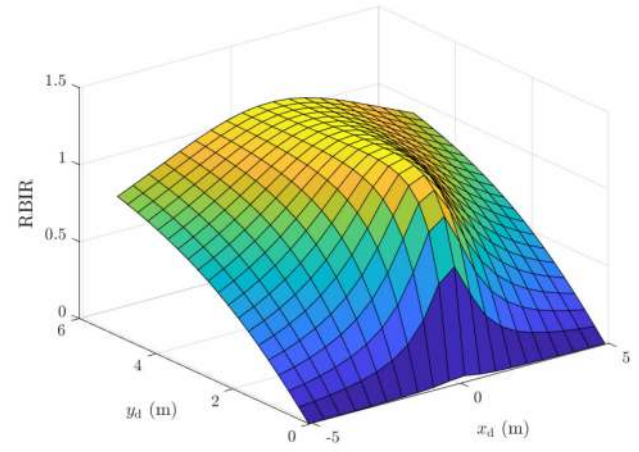


(a) Relative Metasurface to mirror array received power

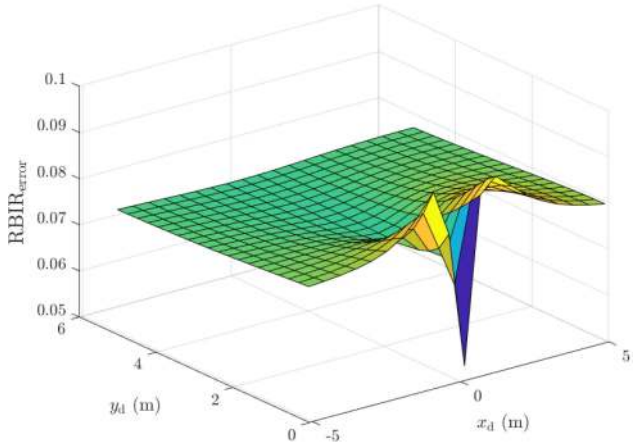


(b) Relative RBIR error

**FIGURE 10.** **The relative reflectors performance vs detector location.**

reflector which prohibits $\theta'_{\bar{\text{R}},\text{Mi}}$ from getting close to $\pi/2$, when the source is not very close to the $x-z$ plane, and keeps it bounded as mentioned previously in Section VII-C. Another important study is to investigate an assessment for the simple analytic formula of (81). Hence, we assess the gain accuracy by studying the relative error metric, $\tilde{G}_{t,\text{error}} \triangleq |\tilde{G}_t - \frac{\tilde{p}^t_{\text{rx}}}{p_{\text{LoS}}}| / \frac{\tilde{p}^t_{\text{rx}}}{p_{\text{LoS}}}$, depicted in Fig. 9(d), Fig. 9(c). The relatively small $\tilde{G}_{\text{MS, error}}$ and $\tilde{G}_{\text{Mi, error}}$ values, supports the use of $\tilde{G}_t$ as a good representative for the more computationally expensive $\frac{\tilde{p}^t_{\text{rx}}}{p_{\text{LoS}}}$ in the assumed regime. To measure the mirror array inter-element blockage effect, in Fig. 9(e) we plot $\tilde{p}^{\text{Mi}}_{\text{rx,error}} \triangleq (\tilde{p}^{\text{Mi}}_{\text{rx,U}} - \tilde{p}^{\text{Mi}}_{\text{rx}})/\tilde{p}^{\text{Mi}}_{\text{rx}}$. It can be seen that, the inter-element blockage effect is significant only when $|\pi/2 - \phi^{\text{Mi}}_{\text{d}}|$, or/and $r^{\text{Mi}}_{\text{d}}$ is small.

In the second example, we visualize the relative performance of the two reflectors in Fig. 10(a), where we plot the RBIR computed by (79), which we use to understand $\frac{\tilde{p}_{\text{rx,MS}}}{\tilde{p}^{\text{Mi}}_{\text{rx,U}}}$. Firstly, we observe from Fig. 10(a), that the mirror array reflector outperforms the metasurface reflector as the projections of $\bar{\text{R}}^{\text{Mi}}\text{D}$, and $\text{S}\bar{\text{R}}^{\text{Mi}}$ in the detector plane deviates angularly from each other. Moreover, the superiority of the mirror array over the metasurface reflector degrades as $r^{\text{Mi}}_{\text{d}}$ increases. These findings are in agreement with the analytical predictions of the RBIR expression (79). Secondly, the validity of the adopted approximation is highly contingent on the small reflector, large $n_t$ assumptions. In Fig. 10(b), we plot the relative discrepancy between the RBIR and $\frac{\tilde{p}_{\text{rx,MS}}}{\tilde{p}^{\text{Mi}}_{\text{rx,U}}}$, represented by $\text{RBIR}_{\text{error}} \triangleq |\text{RBIR} - \frac{\tilde{p}_{\text{rx,MS}}}{\tilde{p}^{\text{Mi}}_{\text{rx,U}}}| / (\frac{\tilde{p}_{\text{rx,MS}}}{\tilde{p}^{\text{Mi}}_{\text{rx,U}}})$. The exhibited relatively small $\text{RBIR}_{\text{error}}$ values in Fig. 10(b), justifies using RBIR as a substitute for $\frac{\tilde{p}_{\text{rx,MS}}}{\tilde{p}^{\text{Mi}}_{\text{rx}}}$ for small reflector regime and large $n_{\text{m}}$ and $n_{\text{p}}$, when mirror array inter-element blockage is negligible.

In the rest of simulations, we study the performance of the exact receievd power computed using (71), (33) and (51), approximated received power based on small detector assumption, using (72), (33) and (51), for $A_{\text{s}} = 10.125\,\text{cm}^2$ and $36.125\,\text{cm}^2$. Moreover, we plot the received power from a point source computed using (72), (65), (62). In addition, we plot the point source approximated Jacobian received power expression for the metasurface reflector computed using (72), (66), and its small reflector simplified counterpart (PSSR) using (72), (67). Also, we plot the received power from point source assuming small mirror array reflector using (72), (63). And finally, we plot the received power for a large source small reflector regime using (72), (69).

In the third simulation, we study the impact of the detector position on the received power from both reflector types. We consider a detector located along the line containing $\tilde{\text{R}}_t$ and making a counter-clockwise angle $\phi^t_{\text{d}}$ with the positive $x-$ axis as shown in Fig. 2 and Fig. 3. We observe that the received power from the metasurface reflector follows a unimodal trend, as shown in Fig. 11(a). This unimodal behavior is well explained by the dominant large $\text{B}SR_{\text{MS}}$ for small $r^{\text{MS}}_{\text{d}}$ and the dominant small solid angle subtended by the detector for large $r^{\text{MS}}_{\text{d}}$. Also, it matches the analytical results presented in (70), for large $n_{\text{p}}$ (proof is omitted for brevity). The asymptotic decreasing received power from the mirror array reflector versus $r^{\text{Mi}}_{\text{d}}$ can be seen clearly from (70) by bounding $\theta^{\text{Mi}}_{\bar{\text{R}}_{\text{Mi}},\text{D}}$, and considering large $n_{\text{m}}$, where all the remaining terms are inversely proportional to $r^{\text{Mi}}_{\text{d}}$ and $\bar{A}_{\bar{\text{R}}_{\text{Mi}}} = w_{\text{m}} h_{\text{m}}$. Moreover, It can be seen in both Fig. 11(a) and Fig. 11(b) that the received power when small and large sources are considered, approach the received powers in the point source and the large source regimes, respectively. Furthermore, it can be seen that the approximated Jacobian point source expression matches the point source curve asymptotically. It is worth mentioning that at $r^{\text{MS}}_{\text{d}} = r^{\text{Mi}}_{\text{d}} = y_{\text{s}}, \phi^{\text{MS}}_{\text{d}} = \phi^{\text{Mi}}_{\text{d}} = 90°$, the received power from both reflectors is almost the same due to the highly symmetric, source, detector, reflector layout. On this occasion, the reflector becomes centered vertically with respect to both the source and the detector and their centers have

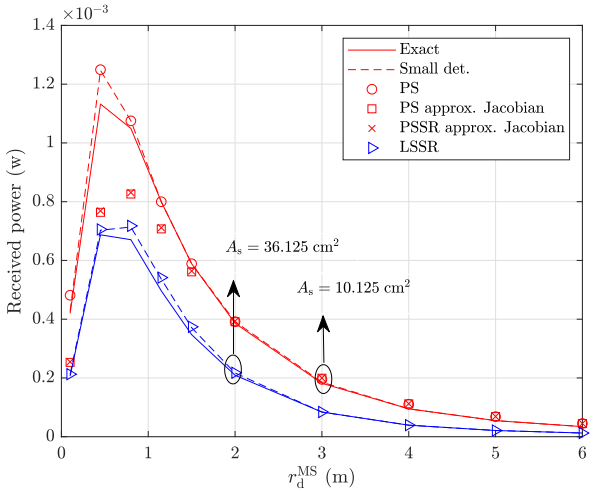


(a) Received power from metasurface reflector vs $r_d^{MS}$

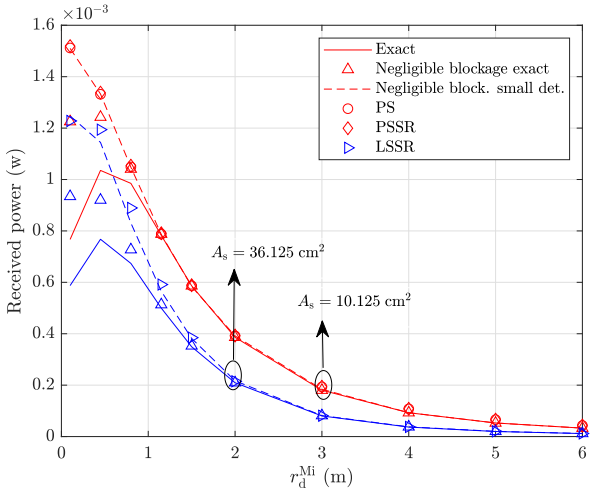


(b) Received power from mirror reflector vs $r_d^{Mi}$

**FIGURE 11.** Received power vs horizontal distance from the reflector center.

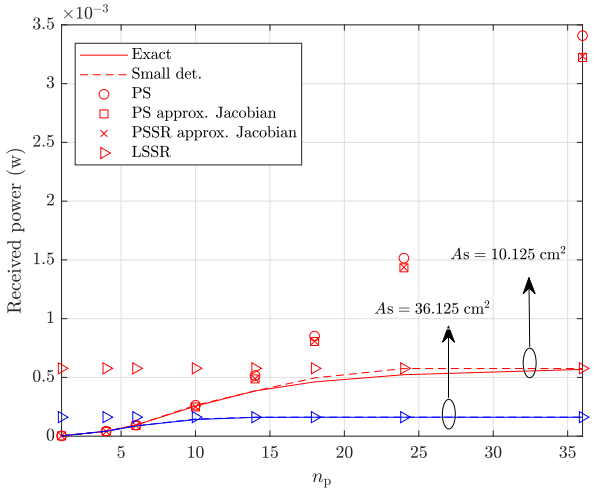


(a) Received power from metasurface reflector vs $n_p$

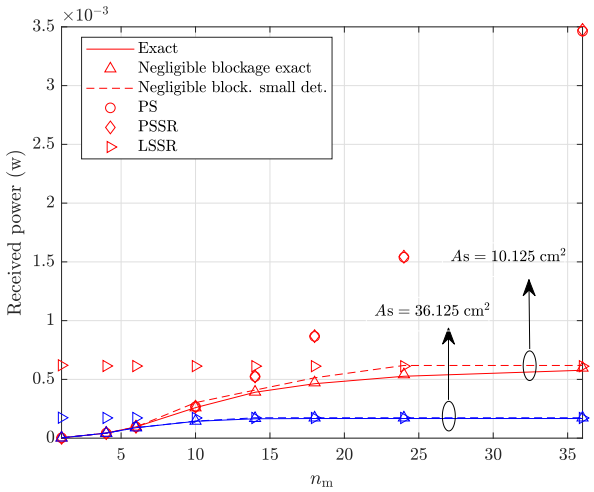


(b) Received power from mirror array reflector vs $n_m$

**FIGURE 12.** Number of reflecting elements impact.

the same $x-$ coordinate. Also, the detector lies right beneath the source; hence, the required phase gradient/tilting angles are approximately zero for all the reflecting elements, and both reflectors perform almost identically.

Finally, we study the impact of the number of reflecting elements on the received power for different source areas, considering a relatively small reflector. Hence, we plot the received power from the metasurface, and the mirror array reflector, respectively, in Fig. 12(a), Fig. 12(b). One can observe that the received power from both reflector types increases with $n_m$ and $n_p$ until a saturation limit. By design, the chief rays hitting the reflectors centers are reflected at the detector center. The coverage area of the source in the detector plane is determined by the set of points in the detector plane intersecting with the reflected rays. This area is the union of the individual reflecting elements coverage areas. For a small reflector, this union can be approximated with any individual coverage area. Individual coverage areas are monotonically increasing with the reflecting elements areas and the source area. As $n_m$ and $n_p$ increase, the reflecting elements areas become smaller, decreasing coverage area and increasing irradiance around the detector center. Consequently, in the asymptotically large $n_m$, $n_p$ regime, the coverage area is determined by $A_s$. The saturation of the received power for large $n_t$ complies with the received power in the LSSR regime where $n_t^2 w_t h_t$ represent the total reflector area (assumed constant). It is observed that the received power from both reflectors in the LSSR regime decreases with $A_s$, which can be noticed from (69). Moreover, the received power from the point source is observed to be monotonically increasing, this is true under the assumption that $n_t$ is not large enough to have significant irradiance variations over the detector surface ((72) will be invalid then). In summary, the received power from both reflectors behaves similar to the point source regime counterpart for small $n_t$ values, and matches its LSSR counterpart for large $n_t$ values.

## IX. CONCLUSION

In this article, we proposed intelligent reflecting surfaces-based VLC systems built using metasurface and mirror array-based reflectors. Throughout our study, we derived irradiance expressions for both reflectors under general relative source, reflectors, detector dimensions, and locations assumptions. Moreover, we derived tractable simplified irradiance expressions for practical special cases, namely, point source, small reflectors, large source small reflector setups at the detector center. Besides, we defined the RBIR metric to evaluate the relative performance of reflectors in terms of received optical power. The proposed metric is a reliable design guide that determines the superior reflector for a particular source, detector, and geometric setup. Furthermore, we derived the received power gain of the reflector-based to the reflector-free LoS based setup, and provided simple upper and lower bound for this gain. As for the focusing capability, we showed analytically it is proportional to the number of the constituting elements till a specific limit; for the small reflector regime. Finally, we quantified the benefits of intelligent surfaces through several numerical examples. Specifically, we found that a 25 cm $\times$ 15 cm reflector can increase the power to five folds or even more than LoS on average.

## APPENDIX A
## RADIANCE OF UNIFORM GENERALIZED LAMBERTIAN EXTENDED SOURCE

Each point on the considered extended source can be thought of as a point source having total radiated power of $\frac{d\Phi}{dA_s}$. By the virtue of the source uniformity assumption, $\frac{d\Phi}{dA_s} = p/A_s$. We assume generalized Lambertian radiation pattern for all the source points with Lambertian order $m$. Hence, the radiated power by each point in a direction defined by a differential solid angle $d\omega$ making an angle $\theta_s$ with the normal to the source can be expressed using [26, eq. (1)] as $\frac{d^2\Phi}{dA_s d\omega} = (m+1)\frac{p}{2\pi A_s}\cos^m(\theta_s)$. Using (5) the required radiance can be expressed as $\frac{d^2\Phi}{dA_s d\omega \cos(\theta_s)} = (m+1)\frac{p}{2\pi A_s}\cos^{m-1}(\theta_s)$, which completes the proof.

## APPENDIX B
## ABSOLUTE REPRESENTATION OF GENERALIZED SNELL'S LAW PROOF

The relation between $i', r'$ and $x, z$ can be deduced from the geometry presented in Fig. 5 as

$$z = i'\cos\left(\phi^i\right) - r'\sin\left(\phi^i\right), \tag{84}$$

$$x = i'\sin\left(\phi^i\right) + r'\cos\left(\phi^i\right). \tag{85}$$

Hence, $\frac{\partial\Theta}{\partial i'}$ and $\frac{\partial\Theta}{\partial r'}$ can be expressed in terms of $\frac{\partial\Theta}{\partial z}$ and $\frac{\partial\Theta}{\partial x}$ as

$$\frac{\partial\Theta}{\partial r'} = -\sin\left(\phi^i\right)\frac{\partial\Theta}{\partial z} + \cos\left(\phi^i\right)\frac{\partial\Theta}{\partial x}, \tag{86}$$

$$\frac{\partial\Theta}{\partial i'} = \cos\left(\phi^i\right)\frac{\partial\Theta}{\partial z} + \sin\left(\phi^i\right)\frac{\partial\Theta}{\partial x}. \tag{87}$$

It can be shown with some geometric and trigonometric manipulations that:

$$\sin\left(\theta^r\right) = \sin\left(\theta'\right)\cos\left(\phi''\right), \tag{88}$$

$$\cos\left(\theta^r\right) = \cos\left(\theta'\right)\sqrt{1+\tan^2(\theta')\sin^2(\phi'')}, \tag{89}$$

$$\sin\left(\phi^r\right) = \tan\left(\theta'\right)\sin\left(\phi''\right)/\sqrt{1+\tan^2(\theta')\sin^2(\phi'')}, \tag{90}$$

where $\phi'' = \phi' - \phi^i$. By substituting (86), (87), (88) , (89) and (90) in (9) and (10), the generalized law of reflection can be re-written as

$$\sin\left(\theta'\right)\sin\left(\phi''\right) = \frac{\lambda}{2\pi n_i}\left(-\sin\left(\phi^i\right)\frac{\partial\Theta}{\partial z} + \cos\left(\phi^i\right)\frac{\partial\Theta}{\partial x}\right), \tag{91}$$

$$\sin\left(\theta'\right)\cos\left(\phi''\right) - \sin\left(\theta^i\right) = \frac{\lambda}{2\pi n_i}\left(\cos\left(\phi^i\right)\frac{\partial\Theta}{\partial z} + \sin\left(\phi^i\right)\frac{\partial\Theta}{\partial x}\right). \tag{92}$$

By multiplying (91) by $\cos\left(\phi^i\right)$, (92) by $\sin\left(\phi^i\right)$, then adding them, we get

$$\sin\left(\theta'\right)\sin\left(\phi''\right)\cos\left(\phi^i\right) + \sin\left(\theta'\right)\cos\left(\phi''\right)\sin\left(\phi^i\right) - \sin\left(\theta^i\right)\sin\left(\phi^i\right) = \frac{\lambda}{2\pi n_i}\frac{\partial\Theta}{\partial x}, \tag{93}$$

which can be re-written as $\sin(\theta')\sin(\phi') - \sin(\theta^i)\sin(\phi^i) = \frac{\lambda}{2\pi n_i}\frac{\partial\Theta}{\partial x}$. Similarly, by multiplying (91) by $-\sin(\phi^i)$, (92) by $\cos(\phi^i)$ then adding them, we obtain

$$-\sin\left(\theta'\right)\sin\left(\phi''\right)\sin\left(\phi^i\right) + \sin\left(\theta'\right)\cos\left(\phi''\right)\cos\left(\phi^i\right) - \sin\left(\theta^i\right)\cos\left(\phi^i\right) = \frac{\lambda}{2\pi n_i}\frac{\partial\Theta}{\partial z}, \tag{94}$$

which reduces to $\sin(\theta')\cos(\phi') - \sin(\theta^i)\cos(\phi^i) = \frac{\lambda}{2\pi n_i}\frac{\partial\Theta}{\partial z}$, which completes the proof.

## APPENDIX C
## METASURFACE BSR PROOF

The considered differential solid angles elements in the spherical coordinate system can be expressed as $d\omega' = \sin(\theta')d\theta' d\phi'$, $d\omega_i = \sin(\theta_i)d\theta_i d\phi_i$. By considering the reflection process as a transformation of variables, the differential area element in the $\theta' - \phi'$ plane $(d\theta' d\phi')$ can be expressed as $d\theta' d\phi' = |J(\frac{\theta',\phi'}{\theta_i,\phi_i})|d\theta_i d\phi_i$. Therefore, $\mathrm{BSR_{MS}}$ at the center of the reflecting element can be expressed as $\mathrm{BSR_{MS}} = \frac{d\omega'}{d\omega_i}|_{\mathrm{R=\bar{R}_{MS}}} = \frac{\cos(\theta_i)}{\sqrt{1-((\sin(\theta_i)\sin(\phi_i)+\frac{\lambda}{2\pi n_i}\frac{\partial\Theta}{\partial x})^2+(\sin(\theta_i)\cos(\phi_i)+\frac{\lambda}{2\pi n_i}\frac{\partial\Theta}{\partial z})^2)}}$ where $\mathrm{I_{\bar{R}_{MS},D}} = \mathrm{S}$. Substituting (11), (12) in the previous equation completes the proof.

## REFERENCES

[1] S. Dang, O. Amin, B. Shihada, and M.-S. Alouini, "What should 6G be?" *Nat. Electron.*, vol. 3, no. 1, pp. 20–29, 2020. [Online]. Available: https://doi.org/10.1038/s41928-019-0355-6

[2] W. Saad, M. Bennis, and M. Chen, "A vision of 6G wireless systems: Applications, trends, technologies, and open research problems," *IEEE Netw.*, vol. 34, no. 3, pp. 134–142, May/Jun. 2019.

[3] J. Zhao and Y. Liu, "A survey of intelligent reflecting surfaces (IRSs): Towards 6G wireless communication networks," 2019. [Online]. Available: arXiv:1907.04789.

[4] Q. Wu and R. Zhang, "Towards smart and reconfigurable environment: Intelligent reflecting surface aided wireless network," *IEEE Commun. Mag.*, vol. 58, no. 1, pp. 106–112, Jan. 2020.

[5] X. Yuan, Y.-J. Zhang, Y. Shi, W. Yan, and H. Liu, "Reconfigurable-intelligent-surface empowered 6G wireless communications: Challenges and opportunities," 2020. [Online]. Available: arXiv:2001.00364.

[6] E. Basar, M. Di Renzo, J. de Rosny, M. Debbah, M.-S. Alouini, and R. Zhang, "Wireless communications through reconfigurable intelligent surfaces," 2019. [Online]. Available: arXiv:1906.09490.

[7] Ö. Özdogan, E. Björnson, and E. G. Larsson, "Intelligent reflecting surfaces: Physics, propagation, and pathloss modeling," *IEEE Wireless Commun. Lett.*, vol. 9, no. 5, pp. 581–585, May 2020.

[8] A. M. Abdelhady, O. Amin, A. Chaaban, B. Shihada, and M.-S. Alouini, "Downlink resource allocation for dynamic TDMA-based VLC systems," *IEEE Trans. Wireless Commun.*, vol. 18, no. 1, pp. 108–120, Jan. 2019.

[9] A. M. Abdelhady, O. Amin, A. Chaaban, B. Shihada, and M.-S. Alouini, "Spectral-efficiency—Illumination pareto front for energy harvesting enabled VLC systems," *IEEE Trans. Commun.*, vol. 67, no. 12, pp. 8557–8572, Dec. 2019.

[10] A. M. Abdelhady, O. Amin, B. Shihada, and M.-S. Alouini, "Spectral efficiency and energy harvesting in multi-cell SLIPT systems," *IEEE Trans. Wireless Commun.*, vol. 19, no. 5, pp. 3304–3318, May 2020.

[11] M. Najafi and R. Schober, "Intelligent reflecting surfaces for free space optical communications," 2019. [Online]. Available: arXiv:1905.01094.

[12] C. Valagiannopoulos, T. A. Tsiftsis, and V. Kovanis, "Metasurface-enabled interference mitigation in visible light communication architectures," *J. Opt.*, vol. 21, no. 11, Oct. 2019, Art. no. 115702.

[13] Z. Cao, X. Zhang, G. Osnabrugge, J. Li, I. M. Vellekoop, and A. M. J. Koonen, "Reconfigurable beam system for non-line-of-sight free-space optical communication," *Light Sci. Appl.*, vol. 8, no. 1, pp. 1–9, Jul. 2019.

[14] P. Deng, M. Kavehrad, and Y. Lou, "MEMS-based beam-steerable FSO communications for reconfigurable wireless data center," in *Broadband Access Communication Technologies XI* (International Society for Optics and Photonics), vol. 10128, B. B. Dingel, K. Tsukamoto, and S. Mikroulis, Eds. Bellingham, WA, USA: SPIE, Jan. 2017, pp. 33–41. [Online]. Available: https://doi.org/10.1117/12.2253342

[15] L. Zou, M. Cryan, and M. Klemm, "Phase change material based tunable reflectarray for free-space optical inter/intra chip interconnects," *Opt. Exp.*, vol. 22, no. 20, pp. 24142–24148, Oct. 2014.

[16] B. Liu, K. Song, and J. Xiao, "Two-dimensional optical metasurfaces: From plasmons to dielectrics," *Adv. Condensed Matter Phys.*, vol. 2019, pp. 1–15, Jan. 2019.

[17] S. M. Kamali, E. Arbabi, A. Arbabi, and A. Faraon, "A review of dielectric optical metasurfaces for wavefront control," *Nanophotonics*, vol. 7, no. 6, pp. 1041–1068, May 2018.

[18] A. Pors, M. G. Nielsen, R. L. Eriksen, and S. I. Bozhevolnyi, "Broadband focusing flat mirrors based on plasmonic gradient metasurfaces," *Nano Lett.*, vol. 13, no. 2, pp. 829–834, Jan. 2013.

[19] Y. C. Cheng *et al.*, "Flat focusing mirror," *Sci. Rep.*, vol. 4, p. 6326, Sep. 2014.

[20] M. Born and E. Wolf, *Principles of Optics: Electromagnetic Theory of Propagation, Interference and Diffraction of Light*. Cambridge, U.K: Cambridge Univ. Press, 1999.

[21] M. S. Rea, *The IESNA Lighting Handbook: Reference & Application*. New York, NY, USA: Illum. Eng. Soc. North America, 2000.

[22] W. R. McCluney, *Introduction to Radiometry and Photometry*. Boston, MA, USA: Artech House, 2014.

[23] P. Dutre, P. Bekaert, and K. Bala, *Advanced Global Illumination*. Boca Raton, FL, USA: AK Peters/CRC Press, 2006.

[24] A. S. Glassner, *Principles of Digital Image Synthesis*, vol. 2. San Francisco, CA, USA: Morgan Kaufmann Publ., 1995.

[25] Z. Ghassemlooy, W. Popoola, and S. Rajbhandari, *Optical Wireless Communications: System and Channel Modelling With MATLAB®*. Milton, ON, Canada: CRC press, 2019.

[26] R. T. Valadas and A. M. de Oliveira Duarte, "Sectored receivers for indoor wireless optical communication systems," in *Proc. 5th IEEE Int. Symp. Pers. Indoor Mobile Radio Commun. Wireless Netw. Catching Mobile Future.*, The Hague, The Netherlands, Sep. 1994, pp. 1090–1095.

[27] J. M. Kahn and J. R. Barry, "Wireless infrared communications," *Proc. IEEE*, vol. 85, no. 2, pp. 265–298, Feb. 1997.

[28] S. Adachi, *The Handbook on Optical Constants of Metals: In Tables and Figures*. Hackensack, NJ, USA: World Sci., 2012.

[29] A. Sarsen and C. Valagiannopoulos, "Robust polarization twist by pairs of multilayers with tilted optical axes," *Phys. Rev. B*, vol. 99, no. 11, 2019, Art. no. 115304.

[30] C. A. Balanis, *Antenna Theory: Analysis and Design*. Hoboken, NJ, USA: Wiley, 2016.

[31] B. E. Saleh and M. C. Teich, *Fundamentals of Photonics*. Hoboken, NJ, USA: Wiley, 2019.

[32] F. Aieta, P. Genevet, N. Yu, M. A. Kats, Z. Gaburro, and F. Capasso, "Out-of-plane reflection and refraction of light by anisotropic optical antenna metasurfaces with phase discontinuities," *Nano Lett.*, vol. 12, no. 3, pp. 1702–1706, 2012.

[33] F. Aieta *et al.*, "Reflection and refraction of light from metasurfaces with phase discontinuities," *J. Nanophotonics*, vol. 6, no. 1, pp. 1–9, Dec. 2012.

[34] S. Marschner and P. Shirley, *Fundamentals of Computer Graphics*. Boca Raton, FL, USA: CRC Press, 2015.


**AMR M. ABDELHADY** (Graduate Student Member, IEEE) received the B.Sc. degree (Hons.) in communications and computer engineering from Cairo University, Giza, Egypt, in 2012, and the M.Sc. degree in electrical engineering from the King Abdullah University of Science and Technology, Thuwal, Saudi Arabia, in 2016, where he is currently pursuing the Ph.D. degree. His general research interests lie in communications theory, signal processing for communications with special emphasis on optical wireless communications systems. Specific research areas include visible light communications, green communications, energy harvesting, and intelligent reflecting surfaces.

**AHMED K. SULTAN SALEM** (Senior Member, IEEE) received the B.S. and M.S. degrees in electrical engineering from Alexandria University, Egypt, and the Ph.D. degree from the Electrical Engineering Department, Stanford University in 2007. He is currently a Senior Lecturer with the King Abdullah University of Science and Technology, Saudi Arabia. His current research interests include energy harvesting, intelligent reflecting surfaces, cooperation, and stochastic geometry in wireless communications.

**OSAMA AMIN** (Senior Member, IEEE) received the B.Sc. degree in electrical and electronic engineering from Aswan University, Aswan, Egypt, in 2000, the M.Sc. degree in electrical and electronic engineering from Assiut University, Assiut, Egypt, in 2004, and the Ph.D. degree in electrical and computer engineering, University of Waterloo, Waterloo, ON, Canada, in 2010.

In June 2012, he joined Assiut University as an Assistant Professor with the Electrical and Electronics Engineering Department. He is currently a Research Scientist with the King Abdullah University of Science and Technology, Thuwal, Saudi Arabia. His general research interests lie in communication systems and signal processing for communications with special emphasis on wireless applications. Specific research areas include optical wireless communication, underwater optical wireless communication, Terahertz communication, green communication, cognitive radio, and molecular communication. He is an Associate Editor for the IEEE COMMUNICATIONS LETTERS and IEEE OPEN JOURNAL OF THE COMMUNICATIONS SOCIETY.

**BASEM SHIHADA** (Senior Member, IEEE) was a Visiting Faculty Member of Computer Science Department, Stanford University. In 2009, he joined the King Abdullah University of Science and Technology, where he is currently an Associate and a Founding Professor of computer science and electrical engineering with the Computer, Electrical and Mathematical Sciences and Engineering Division. His current research covers a range of topics in energy and resource allocation in wired and wireless communication networks, including wireless mesh, wireless sensor, multimedia, optical networks, SDNs, IoT, and cloud computing.

**MOHAMED-SLIM ALOUINI** (Fellow, IEEE) was born in Tunis, Tunisia. He received the Ph.D. degree in electrical engineering from the California Institute of Technology, Pasadena, CA, USA, in 1998. He served as a Faculty Member of the University of Minnesota, Minneapolis, MN, USA, then with the Texas A&M University at Qatar, Doha, Qatar, before joining King Abdullah University of Science and Technology, Thuwal, Saudi Arabia, as a Professor of Electrical Engineering in 2009. His current research interests include the modeling, design, and performance analysis of wireless communication systems.